SMAP Twice-Daily rSIR-Enhanced *EASE-Grid 2.0* Brightness Temperatures

Algorithm Theoretical Basis Document
Version 1.0
July 7, 2020

Mary J. Brodzik[1], David G. Long[2] and Molly A. Hardman[1]

[1] *National Snow and Ice Data Center, Cooperative Institute for Research in Environmental Sciences, University of Colorado, 449 UCB, Boulder, CO, 80309-0449, USA*
[2] *Microwave Earth Remote Sensing Laboratory, Brigham Young University, Provo, UT, USA*

Contents

List of Figures

List of Tables

1 Revision History

Table 1: *Revision History*

Revision	Date	Purpose
1.0	2020-07-07	Initial Revision

2 Acronyms and Abbreviations

Table 2: *List of Acronyms and Abbreviations*

AMSR-E	Advanced Microwave Scanning Radiometer - Earth Observing System
ATBD	Algorithm Theoretical Basis Document
BG	Backus-Gilbert
BYU	Brigham Young University
CDR	Climate Data Record
CETB	Calibrated Passive Microwave Daily EASE-Grid 2.0 Brightness Temperature
CF	Climate and Forecast Metadata Conventions
DAAC	Distributed Active Archive Center
dB	decibel
DIB	Drop-in-the-bucket averaging (used to produce GRD products)
DMSP	Defense Meteorological Satellite Program
EASE-Grid	Equal-Area Scalable Earth Grid (Original Definition)
EASE-Grid 2.0	Equal-Area Scalable Earth Grid Version 2.0
EASE2-M	EASE-Grid 2.0, Mid- and Low-Latitude Cylindrical Projection
EASE2-N	EASE-Grid 2.0, Northern Hemisphere Projection
EASE2-S	EASE-Grid 2.0, Southern Hemisphere Projection
EASE2-T	EASE-Grid 2.0, Temperate and Tropical Cylindrical Projection
EIA	Earth Incidence Angle
EOSDIS	Earth Observing System Data and Information System
ESDR	Earth System Data Record
FCDR	Fundamental Climate Data Record
GHz	GigaHertz
GRD	(Drop-in-the-bucket) Gridding Method
ltod	Local-time-of-day
MEaSUREs	Making Earth System Data Records for Use in Research Environments
MRF	Measurement Response Function
NASA	National Aeronautics and Space Administration
NOAA	National Oceanic and Atmospheric Administration
NORAD	North American Aerospace Defense Command
NSIDC	National Snow and Ice Data Center
NetCDF	Network Common Data Format
rSIR	Radiometer version of SIR

RTM	Radiative Transfer Model
SCP	Scatterometer Climate Record Pathfinder
SDR	Sensor Data Record
SIR	Scatterometer Image Reconstruction
SMMR	Scanning Multichannel Microwave Radiometer
SSM/I	Special Sensor Microwave/Imager
SSMIS	Special Sensor Microwave Imager Sounder
T_B	brightness temperature
TBD	To be determined
TLE	Two-Line Element
UTC	Coordinated Universal Time

3 Purpose of this Document

The Soil Moisture Active-Passive (SMAP) Mission was designed to produce globally-derived soil-moisture maps every 2-3 days. At a spatial resolution of 3-10 kilometers, the soil moisture maps were intended to improve long-range weather and seasonal forecasting, and to set the stage for a new generation of hydrologic models capable of predicting and studying floods and droughts (National Research Council, 2008). The original SMAP mission concept relied on synergistic measurements from both radar and radiometer instruments, with radar information produced at higher spatial resolutions than radiometer measurements. Data products were planned to use both radar and radiometer information to provide higher resolution products (Entekhabi et al., 2010, Entekhabi et al., 2014). Unfortunately, the loss of the radar instrument on July 7, 2015, only six months after launch, compromised the ability to meet spatial resolution mission requirements for soil moisture and freeze-thaw products.

Fortunately, the radiometer version of the Scatterometry Image Reconstruction (rSIR) technique (Long and Daum, 1998, Early and Long, 2001), which has been successfully used to enhance spatial resolution of similar passive microwave sensors (Long and Brodzik, 2016), can be used to enhance the spatial resolution of the SMAP radiometer brightness temperature (T_B) data. Characterized by large fields-of-view and oversampled measurements, SMAP measurements are ideally suited to application of the rSIR technique. This document describes the theoretical basis for application of the rSIR algorithm to improve spatial resolution of gridded SMAP radiometer measurements.

4 rSIR-Enhanced SMAP Product Description

4.1 Product Description

The rSIR-Enhanced SMAP (*rSIR-SMAP*) data product (Brodzik et al., 2019) includes Level 3 gridded, twice-daily, radiometric brightness temperature data for the three SMAP 1.4 GHz radiometer channels (horizontal, vertical and fourth Stoke's parameter). The third Stoke's parameter is used in upstream processing to correct for Faraday rotation caused by the ionosphere and is not included in the gridded data products (Piepmeier et al., 2016). Data are gridded to the EASE-Grid 2.0 Azimuthal and Cylindrical projections (Brodzik et al., 2012, 2014), at various spatial resolutions, as described below. The gridded *rSIR-SMAP* product is archived and distributed by the NASA NSIDC DAAC (http://nsidc.org/data/nsidc-0738).

Input data for the *rSIR-SMAP* product is the the SMAP L1B Radiometer Half-Orbit Time-Ordered Brightness Temperatures, Version 4 (SPL1BTB) data set, minor version R16010 (Piepmeier et al., 2018). Using the quality flag on the input data, only the highest quality SPL1BTB measurements are included in *rSIR-SMAP* product.

4.2 SMAP Instrument

The SMAP instrument is a $6\,\mathrm{m}$ conically-scanning reflector antenna and a common L-band ($1.4135\,\mathrm{GHz}$) feed shared by the radar and radiometer. The reflector rotates about the nadir axis, producing the conically scanning antenna beam with a $3\,\mathrm{dB}$ effective field of view measuring $39\,\mathrm{km} \times 47\,\mathrm{km}$ at an Earth incidence angle of approximately $40°$. The swath width is approximately $1000\,\mathrm{km}$ wide. The radiometer looks in both fore and aft directions (Piepmeier et al., 2017).

The original designs for SMAP products to be produced using both radiometer and radar measurements (Entekhabi et al., 2010) could only be used for the first several months of operations in early 2015. After the failure of the SMAP radar instrument on July 7, 2015, the SMAP radiometer continued to function (Piepmeier et al., 2017). The rSIR algorithm, applied to the radiometer measurements alone, enhances gridded spatial resolution by exploiting irregular patterns of measurement locations and signal oversampling (from large overlaps in adjacent footprints and overlapping swaths).

4.3 Grid Spatial Extent

Azimuthal *rSIR-SMAP* grids extend to the full Northern (EASE2-N) and Southern (EASE2-S) hemispheres, respectively, as described in Brodzik et al. (2012, 2014) (1). The spatial extent of the equal-area cylindrical projections (Figure 3 and Figure 2) is defined to match the extent of compatible grids favored by two user communities: the Mid-Latitude (EASE2-M) grid, extending to $\pm 85.044\,566\,4°$ latitude, has been adopted by the SMAP user com-

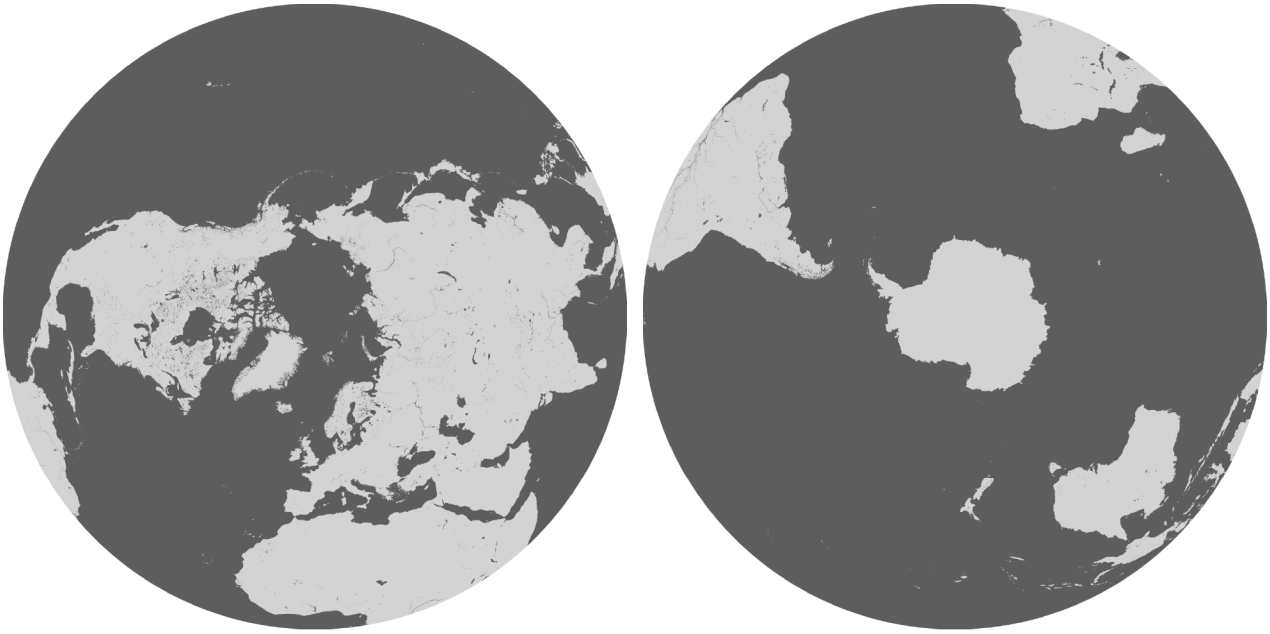

Figure 1: *Northern and Southern EASE-Grid 2.0 projection extents. Land-ocean mask from Brodzik and Knowles (2011).*

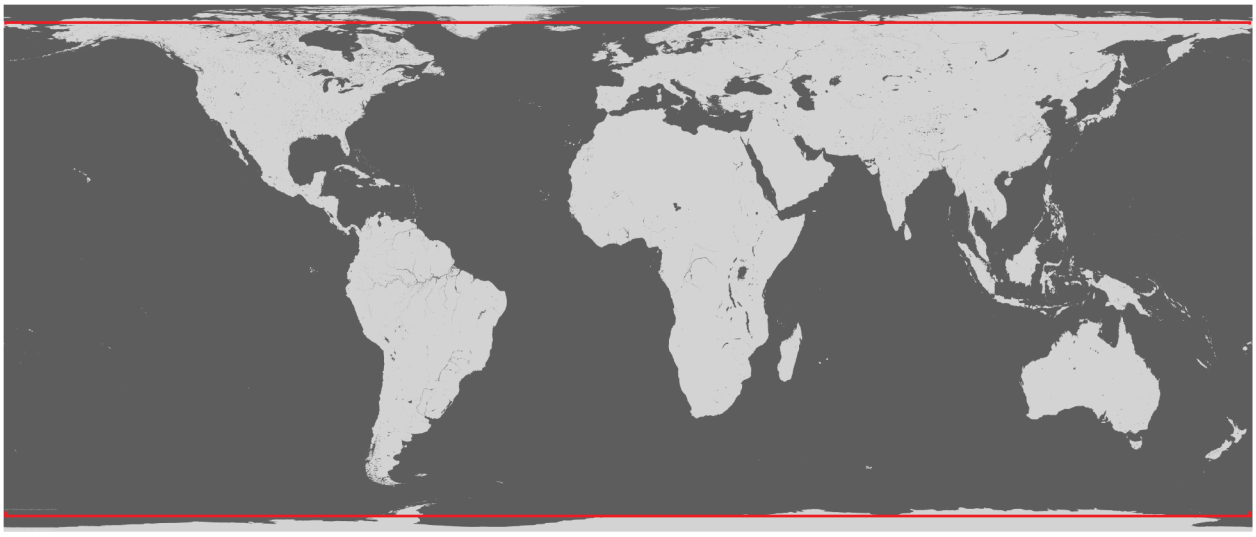

Figure 2: *Cylindrical EASE-Grid 2.0 projection extents. Full extent coverage is EASE2-M, with horizontal red lines delineating the smaller latitudinal extent of EASE2-T grid. Land-ocean mask from Brodzik and Knowles (2011).*

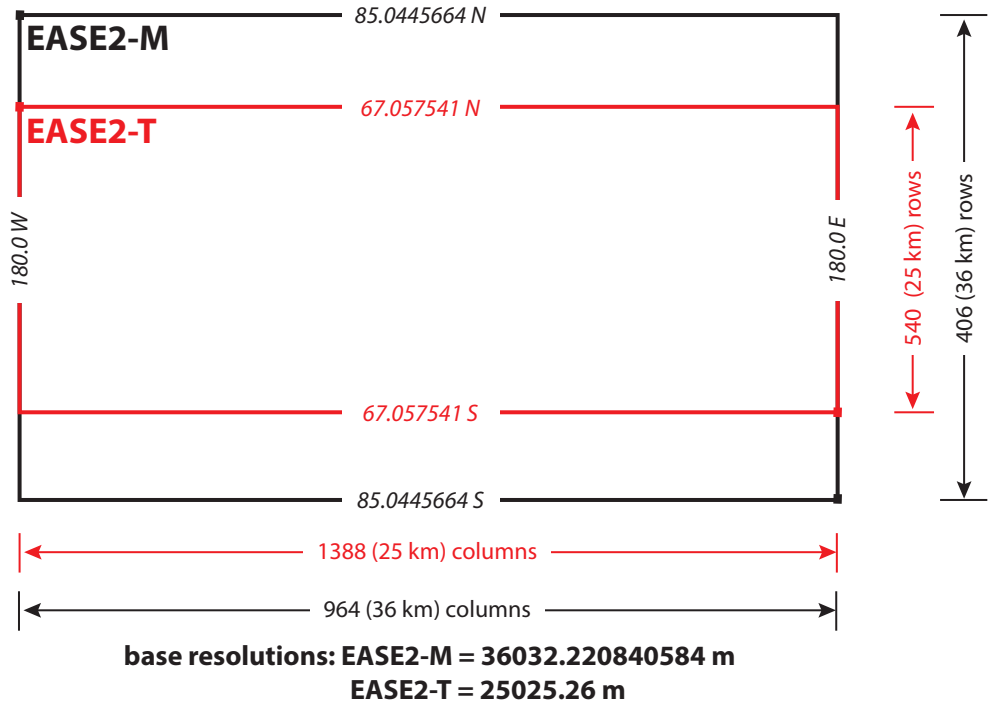

Figure 3: *Relationship of 36 km and 25 km EASE-Grid 2.0 cylindrical projection extents. SMAP EASE2-M extent is defined for compatibility with standard SMAP gridded products. EASE2-T extent is defined for compatibility with CETB products. (Difference in latitudinal extent is exaggerated, see Figure 2 for actual difference in projected extent.) (Brodzik et al., 2019).*

munity; the Temperate and Tropical (EASE2-T) grid, limited to latitudes equatorward of $\pm 67.1°$, is consistent with the original CETB products defined for similar scanning radiometers (Brodzik et al., 2019). See Appendix A, Tables 6 and 7 for grid specifications.

Longitudinal extents of the $36\,\mathrm{km}$ and $25\,\mathrm{km}$ cylindrical grids are identical, with the International Date Line at left and right edges. As with $25\,\mathrm{km}$ *EASE-Grid 2.0* cylindrical grids defined in Brodzik et al. (2012, 2014), the $36\,\mathrm{km}$ cylindrical grids are defined with a nominal cell size of $36\,\mathrm{km} \times 36\,\mathrm{km}$, but actual cell dimensions are slightly larger, as described in Table 6. The cell size adjustment is necessary in order to make the grid exactly span the equator with an integer multiple of cell columns. As a result of these slightly different cylindrical grid cell size differences, the $36\,\mathrm{km}$ and $25\,\mathrm{km}$ cylindrical grids cannot be easily aligned.

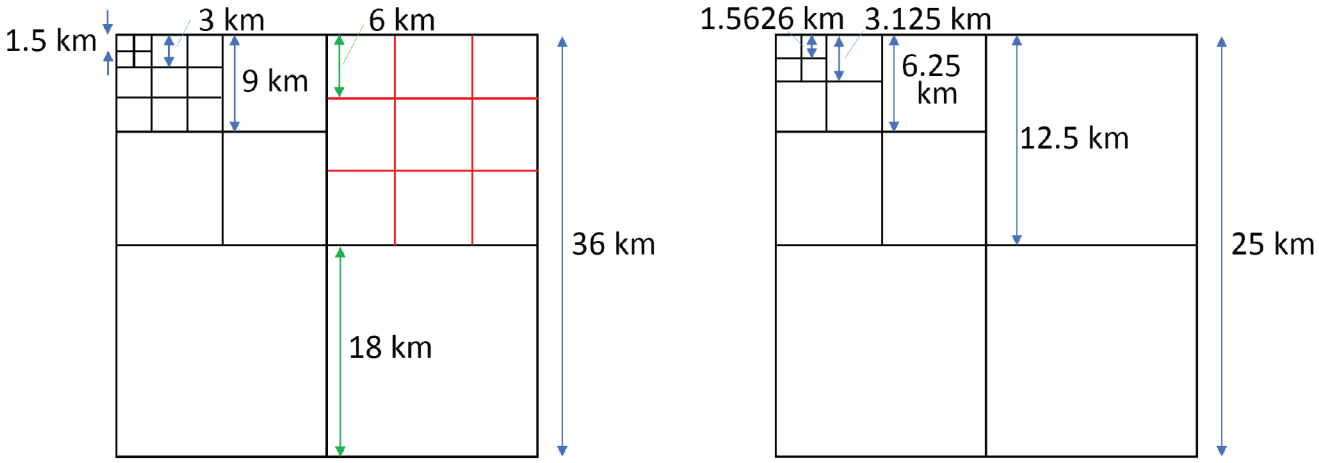

Figure 4: *SMAP divisions of 36 km base resolution cells (left) and 25 km base resolution cells (right). Not all resolutions included in figure are used for processing. (Long et al., 2019).*

4.4 Grid Spatial Resolution

rSIR-SMAP grid resolutions are defined relative to two base resolutions: 1) $36\,\mathrm{km}$ grids and enhanced resolution grids at $9\,\mathrm{km}$ and $3\,\mathrm{km}$, which include EASE2-N, EASE2-S and EASE2-M grids, are compatible with SMAP standard products (Das et al., 2018), and 2) $25\,\mathrm{km}$ grids and the enhanced resolution grid at $3.125\,\mathrm{km}$, which include EASE2-N, EASE2-S and EASE2-T grids, are compatible with the MEaSUREs CETB data products (Brodzik et al., 2019).

The extents of the respective $36\,\mathrm{km}$ and $25\,\mathrm{km}$ *EASE-Grid 2.0* azimuthal grids (EASE2-N and EASE2-S) are exactly identical, due to the fact that the $36\,\mathrm{km}$ and $25\,\mathrm{km}$ cell sizes are both exact divisors of the azimuthal grid extents. Nested resolutions relative to the $36\,\mathrm{km}$ and $25\,\mathrm{km}$ base grids are defined using exact divisors of 2 or 3, as illustrated in Figure 4. rSIR-SMAP projection extents, dimensions and grid cell size details are included in Appendix A. Grids used for *rSIR-SMAP* processing are included in Table 3.

Table 3: *rSIR-SMAP EASE-Grid 2.0 base grids produced, by projection and reconstruction algorithm. See Section 5 for GRD and sSIR reconstruction details.*

EASE2-M	EASE2-N	EASE2-S	EASE2-T
36km (GRD)	36km (GRD)	36km (GRD)	n/a
09km (rSIR)	09km (rSIR)	09km (rSIR)	n/a
03km (rSIR)	03km (rSIR)	03km (rSIR)	n/a
n/a	25km (GRD)	25km (GRD)	25km (GRD)
n/a	3.125km (rSIR)	3.125km (rSIR)	3.125km (rSIR)

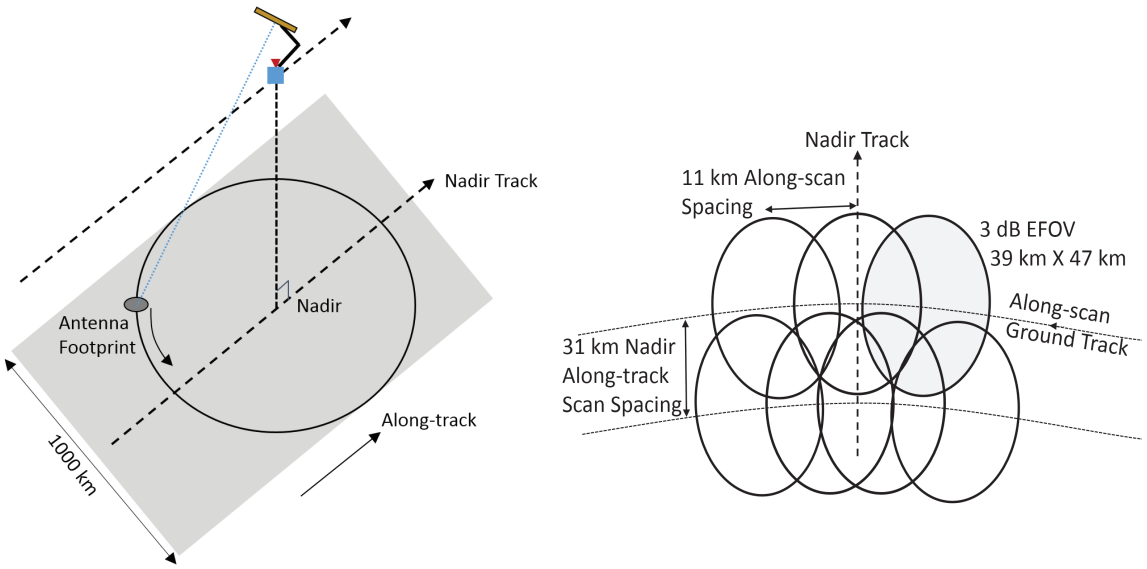

Figure 5: *Illustration of SMAP radiometer swath geometry (left) with antenna and feed rotation about the vertical axis. Incidence angle (not to scale) remains constant as the antenna scans the Earth surface. SMAP radiometer 3 dB antenna footprints (right) for sample measurements along two consecutive antenna rotations. Along-track footprint center spacing is approximately 31 km, with adjacent cross-track spacing approximately 11 km (Long et al., 2019).*

5 Algorithm Description

5.1 Background

Operating at L-band (1.41 GHz) with a 24-MHz bandwidth, the SMAP radiometer collects measurements at horizontal (H), vertical (V), and third and fourth Stokes parameter polarizations with a total radiometric uncertainty of $1.3\,\mathrm{K}$. Launched in January 2015, the SMAP spacecraft flies in a sun-synchronous polar orbit at inclination $98.1°$ and altitude $685\,\mathrm{km}$ (Piepmeier et al., 2016). The SMAP swath and scanning geometry (Figure 5), produces a helical scan pattern on the surface with an along-track spacing of approximately 31 km between antenna rotations.

Vertical (V), horizontal (H), third and fourth Stokes parameter brightness temperature measurements are collected at a nominal incidence angle of $53°$. The polarizations share the same physical aperture, with collocated antenna footprints (Piepmeier et al., 2016). Nominal arrangement of the antenna footprints on the surface for consecutive measurements of two rotations is illustrated in Figure 5.

Image reconstruction techniques such as Backus-Gilbert (Backus and Gilbert, 1967, 1968, 1970) and rSIR (Long and Daum, 1998, Early and Long, 2001) can be applied

to satellite swath data with tuning parameters selected to reduce noise or enhance spatial resolution, but both objectives cannot be achieved simultaneously. The SMAP satellite orbital characteristics, radiometer conical scanning geometry and measurement sampling frequency produce an irregular pattern in measurement locations on the surface that is required for successful spatial resolution enhancement. In a given image, the potential effective spatial resolution enhancement increases in areas with greater overlap, e.g. at higher latitudes. The *rSIR-SMAP* products are produced at diurnal intervals. When data from multiple days can be combined, spatial resolution can be enhanced even more, but at the expense of temporal precision (Long et al., 2020).

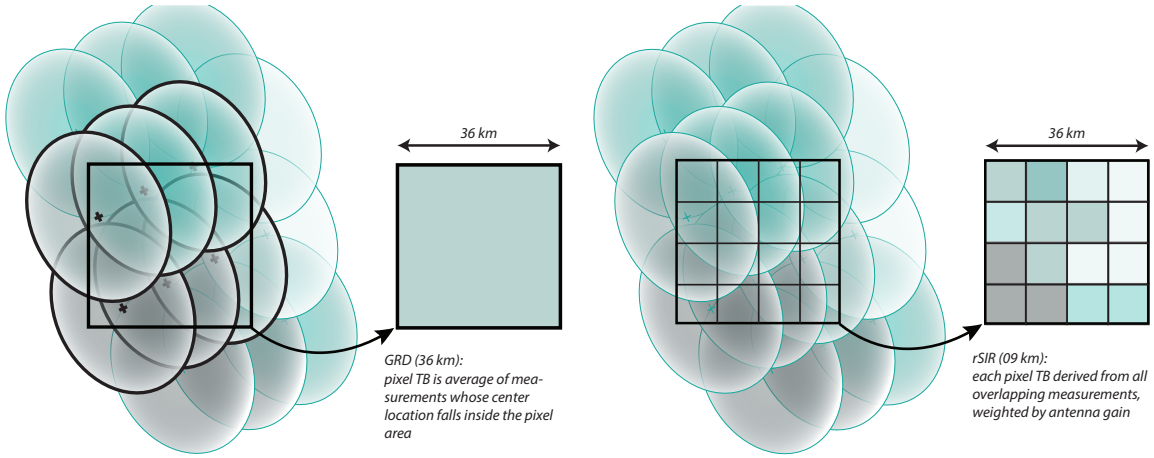

Figure 6: *Simplified illustration of GRD (left) vs. rSIR (right) component measurements with respect to output pixel.*

5.2 rSIR-SMAP GRD Image Products

The *rSIR-SMAP* products include both low-noise (low-resolution) and enhanced-resolution data grids, which can have potentially higher noise (Figure 6). This allows users the flexibility of choosing the gridding method more appropriate for a given research application. For each of the base resolutions ($36\,\mathrm{km}$ and $25\,\mathrm{km}$), each radiometer channel is gridded using conventional drop-in-the-bucket (DIB) unweighted averaging. We refer to these grids as GRD. For the GRD grids, the required information is the location of the measurement. The center of each measurement location is mapped to an output projected grid cell or pixel. The reported GRD T_B value for a given grid cell is calculated from the unweighted average of all measurements mapped to the cell. The effective spatial resolution of the GRD product is defined by a combination of the pixel size and spatial extent of the $3\,\mathrm{dB}$ antenna footprint size (Early and Long, 2001) and has the advantage of not requiring any information

about the antenna pattern (Long and Brodzik, 2016). Since the measurement footprints will extend outside of the pixel area, the effective resolution is coarser than the pixel size. Although the pixel size can be arbitrarily set, the effective resolution is, to first order, the sum of the pixel size plus the larger footprint dimension (Long and Brodzik, 2016).

Finer spatial resolution products are generated using rSIR reconstruction. Long and Brodzik (2016) and Long et al. (2019) have demonstrated that rSIR produces results qualitatively similar to the BG approach while requiring significantly less computation. Both BG and rSIR use regularization to tradeoff noise and resolution. However, BG is based on least squares and depends on a subjectively chosen tradeoff parameter for regularization; rSIR employs maximum entropy reconstruction with regularization accomplished by limiting the number of iterations and thereby only producing partial reconstruction. Computationally, BG employs a potentially large matrix inversion, while rSIR is implemented using iterative methods.

5.3 Radiometer Spatial Response

The effective spatial resolution of enhanced-resolution image products is determined by the spatial measurement response function (MRF) of the sensor and by the image formation algorithm used. The MRF is determined by the antenna gain pattern, the scan geometry (notably the antenna scan angle), and the measurement integration period (Long and Brodzik, 2016).

For T_B image reconstruction, the MRF can be treated as zero everywhere but in the direction of the surface. Microwave radiometers measure the thermal emission, sometimes called the Plank radiation, radiating from natural objects (Ulaby and Long, 2014). In a typical radiometer, an antenna is scanned over the scene of interest and the output power from the carefully calibrated receiver is measured as a function of scan position. The reported signal is a temporal average of the filtered received signal power. The observed power is related to receiver gain and noise figure, antenna loss, physical temperature of the antenna, antenna pattern, and scene brightness temperature (Ulaby and Long, 2014). Because the antenna is rotating during the integration period, the effective antenna gain pattern G_s is a smeared version of the instantaneous antenna pattern G, in the angular direction defined by θ and ϕ, that is,

$$G_s(\theta, \phi) = T_p^{-1} \int_0^{T_p} G(\theta, \phi + \omega_r t) dt \tag{1}$$

where T_p is the integration period and ω_r is the antenna rotation rate. In simplified form, the observed brightness temperature measurement z can be expressed as

$$z = \iint MRF(x, y) T_B(x, y) dx dy + T_{nonSurface} \tag{2}$$

where $T_{nonSurface}$ is the effective brightness temperature contribution from sources not related to the surface brightness temperature distribution $T_B(x, y)$. $MRF(x, y)$ is the MRF expressed in surface coordinates x and y, as

$$MRF(x, y) = G_b^{-1} G_s(x, y) \tag{3}$$

where G_b is the spatially integrated gain over the surface

$$G_b = \iint G_s(x, y) dx dy. \tag{4}$$

Careful calibration and preprocessing estimates and removes $T_{nonSurface}$ from the measurements. The image formation estimates the surface brightness temperature map $T_B(x, y)$ from the calibrated measurements z.

5.4 Image Reconstruction

The goal of image reconstruction is to estimate the surface $T_B(x, y)$ from the sensor T_B measurements. The nominal resolution of the T_B measurements is typically considered to be the size of the $3\,\mathrm{dB}$ response pattern of the MRF. Although the effective resolution of DIB imaging is no finer than the effective resolution of the measurements, reconstruction techniques can yield higher effective resolution if spatial sampling requirements are met.

Measurements from a single channel that are combined into a given output pixel may have different incidence angles (though the incidence angle variation is small) and azimuth angles relative to north (the orientation of the footprint ellipse as projected on the Earth surface). Measurements from multiple orbit passes over a narrow local time window may also be combined. When multiple measurements are combined, the resulting images represent a temporal average of the measurements over the averaging period. There is an implicit assumption that the surface characteristics remain constant over the imaging period and that T_B does not depend on the azimuth angle of the observation. (This is true for most surfaces, but not all, for example, snow and sand dunes or plowed fields.) For both conventional-resolution (GRD) and enhanced-resolution (rSIR) images, the effective gridded image resolution depends on the number of measurements and the precise details of their overlap, orientation, and spatial locations.

In the reconstruction algorithms, the MRF for each measurement is used in estimating the surface T_B on a fine-scale grid. As previously noted, the MRF is determined by the antenna gain pattern, the scan angle geometry, and the measurement integration period. The MRF describes how much the emissions from a particular location on the surface contribute to the observed T_B value. For image formation, T_B is computed at each pixel on the *EASE-Grid 2.0* grid. If the measurement sampling pattern were uniform on this grid, classic reconstruction and deconvolution techniques could be used. However, actual measurement

locations are not aligned with the Earth-centered grid, which results in an irregular sampling pattern. Thus, signal reconstruction based on irregular sampling is applied.

If full signal reconstruction were employed, noise in the signal measurements could be excessively amplified. We therefore limit the computation to produce partial reconstruction by regularization, which imposes a smoothing constraint on the reconstructed image and prevents extreme values. The rSIR has proven effective in generating high-resolution brightness temperature images (Long and Daum, 1998, Long and Brodzik, 2016). rSIR provides results superior to the Backus–Gilbert method, with significantly less computation (Long and Brodzik, 2016). Regularization is built into both BG and rSIR to enable a tradeoff between signal reconstruction accuracy and noise enhancement. To enable computational comparison, we have implemented both BG and rSIR and include performance comparisons in Section [TBD]. We note that BG is used to enhance SMAP spatial resolution by Chaubell et al. (2017), who describe the high computational load, and chose an implementation that uses several geometric approximations and limits the number of input measurements.

Both BG and rSIR techniques can estimate surface brightness on a finer grid than is possible with the conventional DIB approach, i.e., the resulting brightness temperature estimate has a finer effective spatial resolution than DIB methods. As a result, the images are often called *enhanced resolution*, though, in fact, the reconstruction algorithm merely exploits the available information to reconstruct the original signal at higher resolution than DIB gridding, based on the assumption of a bandlimited signal (Early and Long, 2001). The potential resolution enhancement depends on the sampling density at the particular location and the MRF; however, improvements of 25–1000% in the effective resolution have been demonstrated in practice for particular applications. For radiometer enhancement, the effective improvement in resolution tends to be limited, and, in practice, is typically less than $100\,\%$ (see Appendix C). Nevertheless, the resulting images have improved spatial resolution and information content. Note that in order to meet Nyquist requirements for the signal processing, the pixel resolution of the images must be finer than the effective resolution by at least a factor of 2. When multiple passes over an area are combined, reconstruction algorithms intrinsically exploit the resulting oversampling of the surface to improve the effective spatial resolution in the final image. For comparison, note that the effective resolution for DIB gridding is essentially the sum of pixel grid size plus the spatial dimension of the measurement, which is typically defined by the half-power, or the $3\,\mathrm{dB}$ beamwidth. Based on Nyquist considerations, the highest representable spatial frequency for DIB gridding is twice the grid spacing.

5.5 rSIR Method

By contrast with BG methods that require computationally expensive matrix inversion techniques, rSIR is an iterative technique. In the reconstruction the surface brightness temperature distribution $T_B(x, y)$ is treated as a discrete signal sampled at the map pixel spacing

and is estimated from the noisy measurements z. The implementation approach is to vectorize T_B over an $N_x \times N_y$ pixel grid into a single dimensional variable $a_j = T_B(x_j, y_j)$, where $j = l + N_x k$. A particular calibration-corrected measurement z_i can be expressed as

$$z_i = \sum_{j \in image} h_{ij} a_j \tag{5}$$

where $h_{ij} = MRF(x_l, y_k)$ is the discretely sampled measurement evaluated at the jth pixel center. The MRF is typically negligible some distance from the measurement, so the sum is only computed over an area local to the measurement position. The h_{ij} are normalized so that $\sum_j h_{ij} = 1$. Changing to matrix notation for the collection of available measurements, Equation (5) becomes

$$\vec{T} = \mathbf{H}\vec{a} \tag{6}$$

where $\mathbf{H}$ contains the sampled MRF for each measurement, and $\vec{T}$ and $\vec{a}$ are vectors composed of the measurements z_i, and the sampled surface brightness temperature a_j, respectively. The matrix $\mathbf{H}$ is sparse, and may be overdetermined or underdetermined depending on the sampling density.

The rSIR algorithm iteratively solves Equation (6) (Long and Daum, 1998). It approximates a maximum-entropy solution to an underdetermined equation and a least-squares solution to an overdetermined system. The first iteration of rSIR, termed *AVE* (for weighted *AVE*rage), is a simple estimate of T_B with the jth pixel given by

$$a_j^0 = \frac{\sum_i h_{ij} z_i}{\sum_i h_{ij}}. \tag{7}$$

At the kth ($k > 0$) iteration of rSIR, we define the forward projection f_i^k and scale factor d_i^k as

$$f_i^k = \frac{\sum_n h_{in} a_n^k}{\sum_n h_{in}} \tag{8}$$

$$d_i^k = \sqrt{\frac{z_i}{f_i^k}} \tag{9}$$

where n is the index to each pixel in the image. The nonlinear update term u_{ij}^k is

$$u_{ij}^k = \begin{cases} \left[\frac{1}{2f_i^k}\left(1 - \frac{1}{d_i^k}\right) + \frac{1}{a_j^k d_i^k}\right]^{-1}, & \text{if } d_k^k \geq 1 \\ \left[\frac{1}{2} f_i^k \left(1 - d_i^k\right) + a_j^k d_i^k\right], & \text{if } d_k^k < 1 \end{cases} \tag{10}$$

and the jth image pixel is computed as

$$a_j^{k+1} = \frac{\sum_i h_{ij} u_{ij}^k}{\sum_i h_{ij}}. \tag{11}$$

This set of equations is iterated over k for N iterations. Following Long et al. (2019), we minimize computations by defining "nearby" pixel measurements to be regions where the MRF is within $8\,\mathrm{dB}$ of the peak response. The MRF is set to zero elsewhere. For each output pixel and channel, the T_B is calculated using the measurement geometry of the antenna pattern rotated to the Earth azimuth scan angle. This increases computational load, but accounts for the elliptical shape of the footprint and the variation of of measurement locations in grid cells, producing the best quality images.

5.6 rSIR Performance Simulation

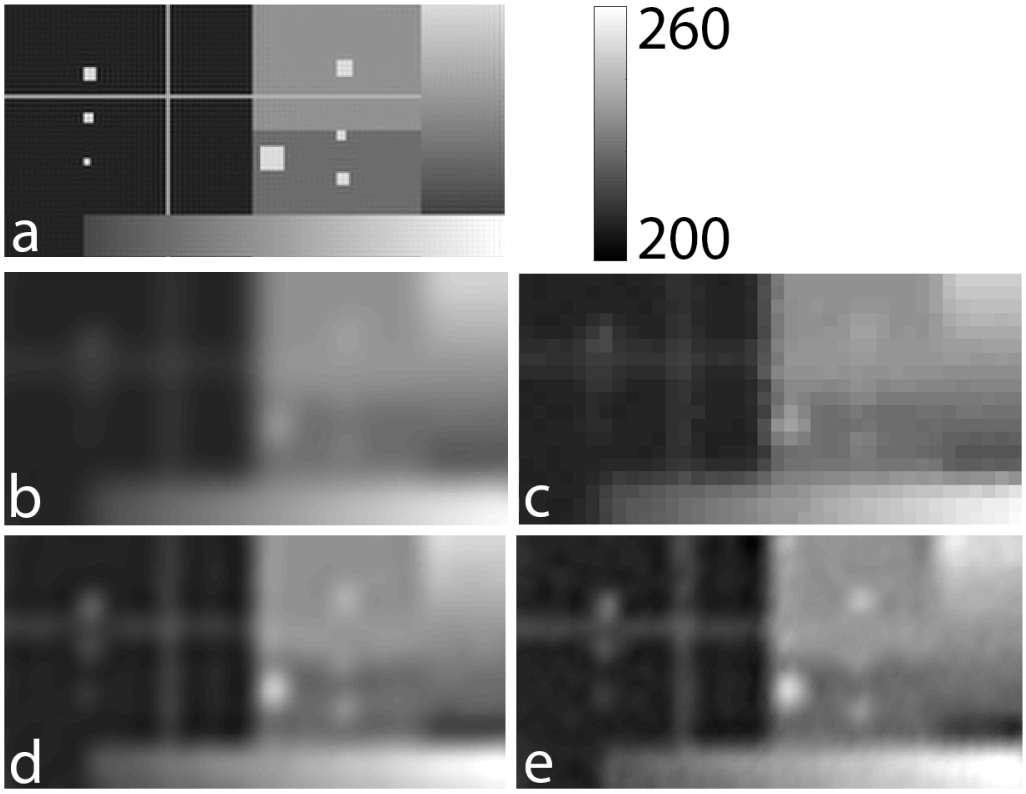

Figure 7: *T_B images from different methods. (a) "True" simulation image. The true image has been band-pass filtered to 10 km effective resolution. (b) AVE (first iteration of rSIR, N = 1). (c) DIB (25 km). (d) rSIR after N = 20 iterations. (d) BG with $\gamma = 0.425\pi$. (Long et al., 2019).*

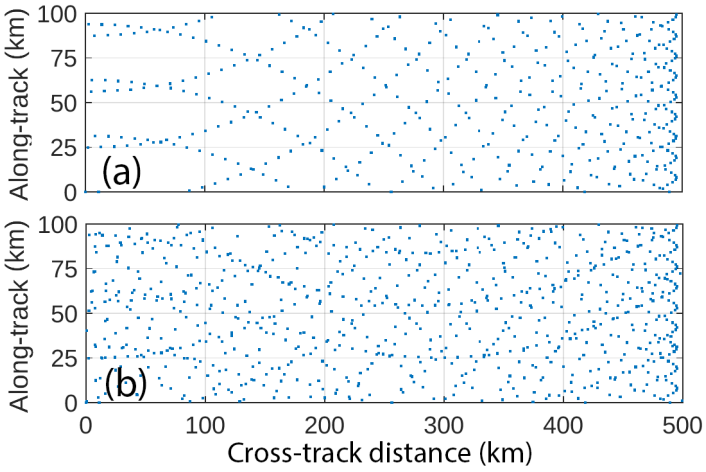

Figure 8: *Illustration of measurement locations within a small area of a SMAP swath: locations for a single pass (a), and locations for two consecutive passes (b). Axis labels for along-track and cross-track distance are oriented relative to first pass (Long et al., 2019).*

We use simulation to evaluate the rSIR algorithm performance simulation, and to evaluate tradeoffs in selecting algorithm parameters for output pixel size and number of iterations. As described in Long et al. (2019), we define a simplified, but still realistic, simulation of the SMAP geometry using an idealized MRF to generate measurements of a synthetic, Earth-centered image. From both noisy and noise-free measurements, DIB, AVE, rSIR, and BG images are created, with error (mean, and root-mean-square [rms]) determined for each case. The measurements are assumed to have a standard deviation of $\pm 1\,\mathrm{K}$; results are relatively insensitive to the standard deviation value used. The same simulated measurements are used for both BG and rSIR. Two pass cases are considered: the single-pass case and the case with two overlapping passes. The simulation shows that the relative performance of rSIR and BG are the same for both cases. Since multiple passes are often combined, the two-pass case is emphasized in the simulations presented. An arbitrary "truth" image is generated with representative features including spots of varying sizes, edges, and areas of constant and gradient T_B (image (a) in Figure 7. Based on the SMAP measurement geometry, simulated locations of antenna bore-site at the center of the integration period are plotted in Figure 8 for both a single pass and two passes.

Long and Brodzik (2016) analysed the rSIR reconstruction accuracy relative to the accuracy of the MRF, determining that, when used for only partial reconstruction, rSIR is tolerant to errors in describing the MRF. Therefore, a simplified model for the MRF can be used. The SMAP MRF is modeled with a 2-D Gaussian function whose $3\,\mathrm{dB}$ (half-power) matches the footprint size. The orientation of the ellipse varies over the swath according to the azimuth antenna angle. To apply the MRF in the processing, the MRF is positioned at the center of the nearest neighbor pixel to the measurement location and oriented to align

with the azimuth antenna angle. The values of the discrete MRF are computed at the center of each pixel in a box surrounding the pixel center. The size of the box is defined to be the smallest enclosing box for which the sampled antenna pattern is larger than a minimum gain threshold of $30\,\mathrm{dB}$, relative to the peak gain. For SMAP, the box size is $125\,\mathrm{km}$. A second threshold (typically $8\,\mathrm{dB}$) defines the gain cutoff used in the rSIR processing. The latter threshold defines the N_{size} parameter used by Long and Daum (1998) and is the same value used in the CETB for other satellite radiometers.

The image pixel size defines how well the MRF can be represented in the reconstruction processing and the simulation. Figure 9 illustrates representative plots of the MRF sampling for each pixel size under consideration, relative to the $25\,\mathrm{km}$ base grids. Analogous MRFs are also generated relative to the $36\,\mathrm{km}$ base grids. As the pixel size is decreased, the sampled MRF more closely resembles a continuous MRF, thereby reducing quantization error; however, smaller pixel sizes increase computational load and the size of output products. Finer resolution results in smoother images on a finer posting grid. To meet Nyquist requirements, image results must be posted at least twice the highest frequency component of the signal.

Separate images are created for both noisy and noise-free measurements. Error statistics (mean, standard deviation, and rms) are computed from the difference between the "truth" and estimated images for each algorithm option. The noise-only rms statistic is created by taking the square root of the difference of the squared noisy and noise-free rms values. DIB images are created by collecting and averaging all measurements whose center falls within each base pixel size grid element. For comparison with high-resolution rSIR images, the DIB image is pixel-replicated to match the pixels of the rSIR images.

Table 4: *Error statistics for 1- and 2-pass simulations on the* $25\,\mathrm{km}$ *(DIB) and nested* $3.125\,\mathrm{km}$ *(AVE, BG, rSIR) images. rSIR uses* $N = 30$ *iterations. BG uses* $\gamma = 0.425\pi$ *(Long et al., 2019).*

Case	Passes	Mean	Std Dev	RMS
DIB	1	-0.19	6.10	6.10
AVE	1	0.00	6.20	6.20
BG	1	-0.48	5.61	5.63
rSIR	1	0.02	5.12	5.12
DIB	2	-0.22	6.13	6.13
AVE	2	-0.02	6.08	6.10
BG	2	-0.27	5.28	5.28
rSIR	2	0.01	5.16	5.16

Figure 7 illustrates a typical simulation result for the dual pass case, with true image and various options for noisy image estimates. The error statistics for this case are given in Table 4. For this example, the image size is 448×224 pixels, with $3.125\,\mathrm{km}$ pixels. For most

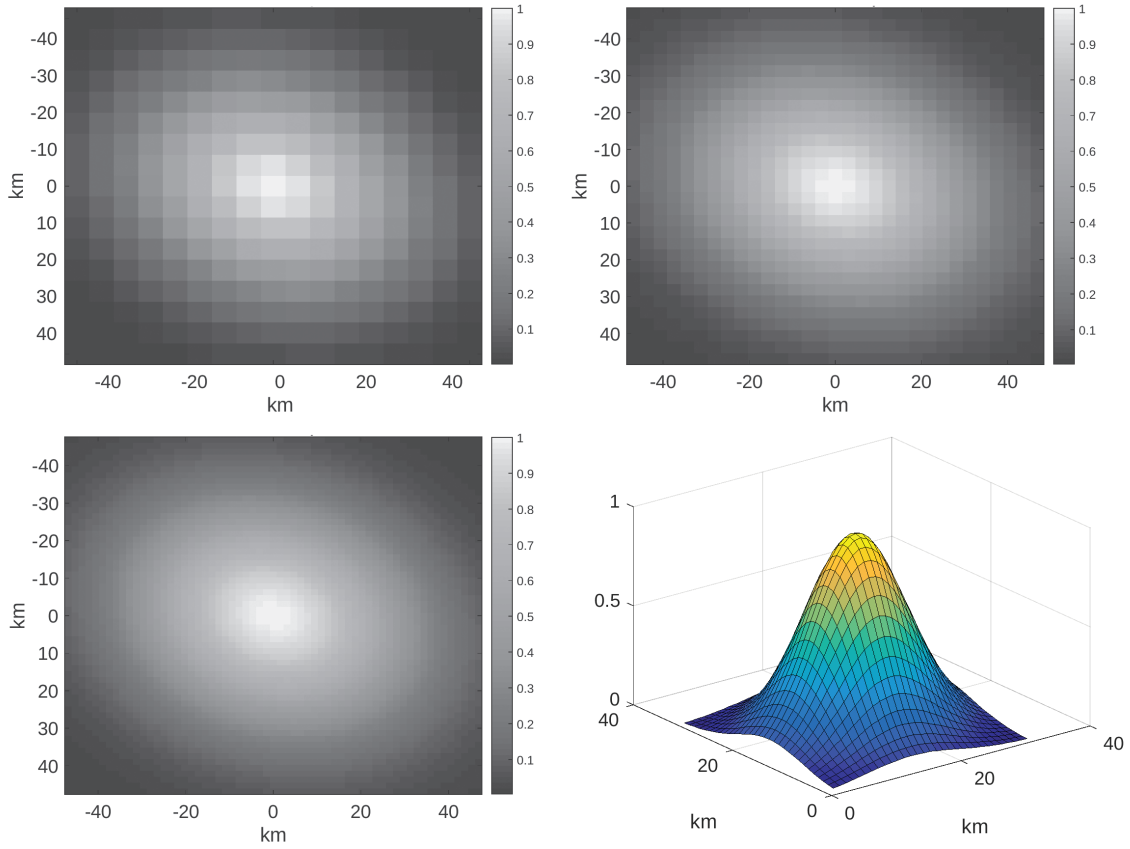

Figure 9: *Sampled MRF plots for potential reconstruction pixel sizes relative to 25 km base grids: 6.25 km (top left), 3.125 km (top right), 1.5625 km (bottom left), with perspective view of 3.125 km MRF (bottom right) Long et al. (2019).*

Table 5: *rSIR simulation error statistics by pixel size for 2-pass simulations with $N = 30$ iterations. (Long et al., 2019).*

Grid	Size	Mean	Std Dev	RMS
CETB	1.526	0.04	5.14	5.14
CETB	3.125	0.01	5.16	5.16
CETB	6.25	0.02	5.12	5.12
CETB	12.5	0.01	3.93	3.93
CETB	25	0.03	3.00	3.00
SMAP	1.5	0.01	5.12	5.12
SMAP	3	0.02	5.14	5.14
SMAP	6	0.01	5.31	5.31
SMAP	9	0.02	4.27	4.27
SMAP	12	0.03	3.95	3.95
SMAP	18	0.01	3.61	3.61

cases, the error is effectively zero mean. For all cases, multiple passes have the smallest error. In general, rms error is the smallest for the rSIR results, followed by BG. Visually, DIB and AVE are similar, while rSIR images better define edges. The spots are much more visible in the rSIR and BG images than in the DIB images, though the rSIR and BG images produce a higher apparent noise "texture". The BG image resembles the rSIR image but is noisier.

5.6.1 rSIR Selection of Pixel Size

Table 5 compares simulation error by pixel size for both CETB and SMAP standard grids. Results quantify the expected tradeoff between pixel size and noise level. Comparing similar pixel sizes from the different base grids suggests that the projection choice has only a very limited effect: the pixel size is the most critical factor. Larger pixel sizes will minimize computational load; however, finer pixels are desired to exploit the finer resolution possible with the reconstruction. For CETB, to ensure compatibility with the grid sizes chosen for other sensors, we adopt the $3.125\,\mathrm{km}$ processing grid. Noting that the error is smaller for $3\,\mathrm{km}$ grid elements than for $6\,\mathrm{km}$ elements, we adopt the $3\,\mathrm{km}$ grid size for the SMAP grid product. For consistency with standard SMAP products, we also include the $9\,\mathrm{km}$ grid size.

5.6.2 rSIR Optimum Number of Iterations

Long and Brodzik (2016) demonstrated the tradeoff between reconstruction accuracy and noise, noting that truncation of the rSIR iteration is useful minimize overall error. To understand the tradeoff between the number of iterations and signal and noise, Figure 10

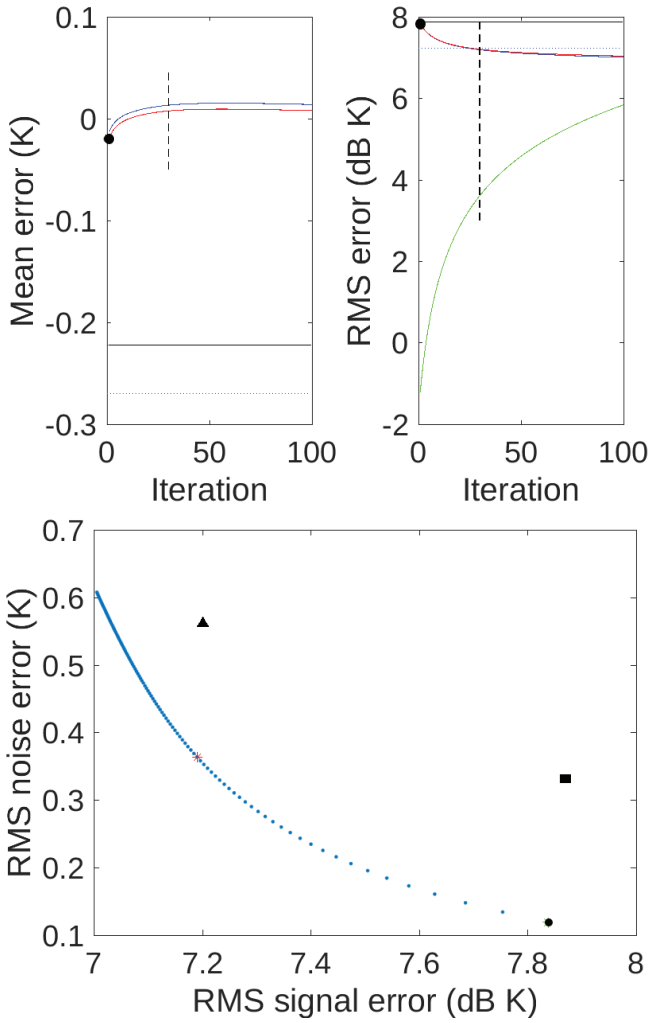

Figure 10: *rSIR reconstruction error statistics by iteration number: mean error (top left), RMS error (top right), and RMS noise power versus RMS signal error by iteration (bottom). Red line is noisy measurement case; blue line is noise-free case. Green line is noise power computed from the difference between the noisy and noise-free cases, which is vertically displaced for clarity. The large spot is error for the AVE (rSIR with $N = 1$) image. The optimum (minimum error) number of iterations occurs at the minimum of the red curve in the RMS error plot. For reference, the vertical dashed line is shown at rSIR $N = 20$ iterations. The horizontal dotted line shows the optimum (minimum) BG value ($\gamma = 0.425\pi$), while the solid line is the DIB value. In bottom plot, rSIR iteration results begin with AVE ($N = 1$, large black dot) in lower right, proceeding with increasing N to upper left with $N = 20$ indicated by red star, compared with DIB (large square) and BG for optimum γ (black triangle). Note that rSIR has similar signal error to BG but lower noise (Long et al., 2019).*

demonstrates tradeoffs between number of iterations N with signal and noise, including similar scores for DIB and AVE (rSIR for $N = 1$) images. As the number of iterations is increased, the images sharpen and details become more evident (i.e. signal rms error decreases). However, the noise level also increases with increasing iteration. Thus, while the iteration improves the signal, excessive iteration can overly enhance the noise. Noting that we can stop the rSIR iteration at any point, we somewhat arbitrarily choose a value of 20 iterations, which provides good signal performance and only slightly degraded the noise performance. This is the value used in Table 4, where the overall error performance of the rSIR reconstruction is better than the DIB and BG results.

To understand the effects of grid size, the simulations were repeated for different values of N and different number of passes. While particular numerical values of RMS error changed, overall rankings and relative spacing of DIB, rSIR and BG values are the same for all cases, and are consistent with values calculated for other satellite radiometers (Long and Brodzik, 2016). Results can be summarized as follows:

1. For a wide range of the rSIR number of iterations, the error and resolution performance of rSIR is better than DIB. rSIR provides better effective resolution than DIB, and
2. Based on the rms error comparison, the performance of rSIR is slightly better than BG with the optimum γ. Therefore, rSIR is preferred over BG.

5.6.3 Local-Time-of-Day

The microwave brightness temperature is the product of surface physical temperature and surface emissivity. As a result of the SMAP sun-synchronous orbit geometry, the radiometer observations at a given location on the earth fall within two narrow diurnal windows. At the equator, these correspond to the ascending and descending orbit passes. The *rSIR-SMAP* images on the cylindrical *EASE-Grid 2.0* projections are separated by ascending and descending passes.

Near the poles, the temporal windows widen to several hours but remain relatively narrow. Since surface temperatures can fluctuate widely during the day, daily averaging is not generally useful at these locations, since it smears diurnal temperature fluctuations in the averaged T_Bs. However, it is reasonable to split the data into two distinct images per day, using intervals based on local-time-of-day (ltod), thereby only combining measurements with a similar ltod. This minimizes the fluctuations in the observed T_B at high latitudes due to changes in physical temperature from daily temperature cycling.

The *rSIR-SMAP* images on the azimuthal projections are separated into twice-daily, morning and evening passes based on observation ltod. At low latitudes, which typically have few overlapping swaths at similar ltod in the same day, ltod division is equivalent to ascending/descending division. An ancillary data array is included in each file, to describe the effective time average of the measurements combined into the pixel for a particular

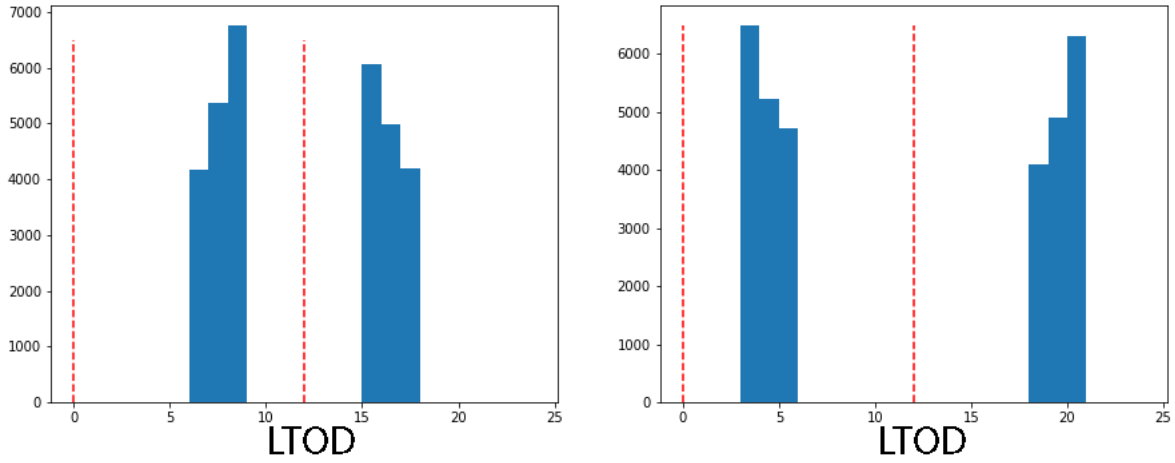

Figure 11: *Histograms of typical measurement ltod for SMAP radiometer measurements falling within a* $1°$ *latitude band at* $70°$–$71°$ *N (left) and* $70°$–$71°$ *S (right) for July 3, 2015. All measurements fall into only one of two narrow ltod time periods, centered at approximately 08:00 or 16:00 h in the Northern Hemisphere, and 04:00 or 20:00 h in the Southern Hemisphere. Although the center time varies with latitude, any point on Earth is observed at one of two times within* $\pm 90\,\mathrm{min}$ *of the times depicted here. Long et al. (2019).*

day. This enables investigators to explicitly account for the ltod temporal variation of the measurements included in a particular pixel.

Histograms of the ltod SMAP radiometer measurements falling within two narrow high-latitude bands (± 70–71) are shown in Figure 11. For the SMAP platform orbital position, a natural division in the measurement ltod is at 00:00 and 12:00 h. For consistency with Long and Brodzik (2016) and Brodzik et al. (2019), the *rSIR-SMAP* data are produced using this ltod division. The SMAP orbit did not drift during the first three years of operation included in the processing. For forward processing, the ltod division time can be adjusted if necessary to account for possible orbital drift (Brodzik and Long, 2018).

5.7 Sample Data

Figure 12 contains sample subsets of *rSIR-SMAP* data extracted from the full EASE-Grid 2.0 Northern Hemisphere grid for DIB, rSIR, with BG images included for comparison purposes. Visual comparison of the images reveals improved detail in the rSIR and BG images compared to the DIB images. As expected, the DIB images are blocky, while the high-resolution images exhibit finer resolution. Subjectively, the rSIR images have the highest contrast and appear more detailed than the BG images. The BG images exhibit greater texturing and noise compared to the rSIR images.

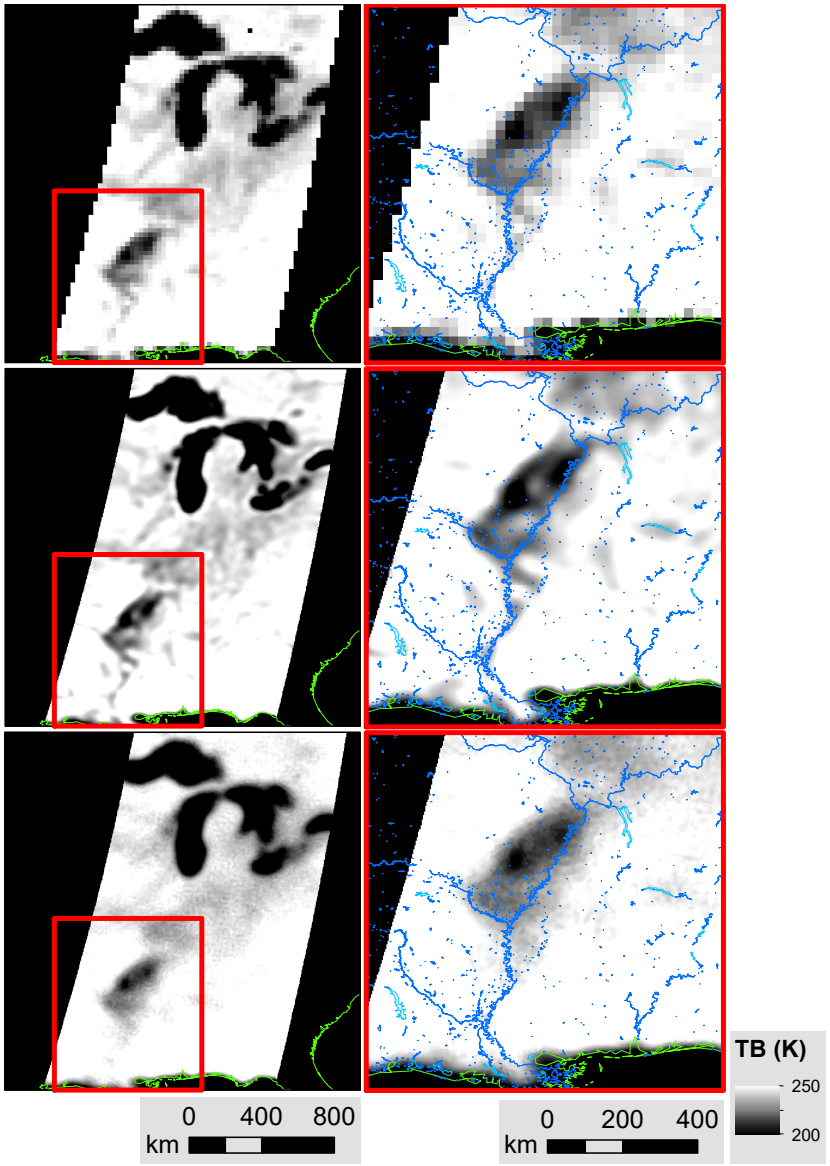

Figure 12: *Northern Hemisphere SMAP Radiometer EASE-Grid 2.0 1.4 GHz, vertically polarized, brightness temperature images, morning overpasses, day of year 092, 2015, demonstrating spatial resolution enhancement from (Top row) 25 km DIB to (Center row) 3.125 km rSIR, and (Bottom row) 3.125 km BG. The left column shows the U.S. Midwest Mississippi Valley, from the Great Lakes to the Gulf of Mexico, with coastlines in green (Wessel and Smith, 2015). The right column is magnified area of respective DIB, rSIR, and BG images, with lakes and wetlands in blue (Lehner and Döll, 2004). Note colder brightness temperature area evident along Mississippi Valley, with greater detail in rSIR and BG image reconstructions (Long et al., 2019).*

5.8 Data Volume

Individual file sizes vary due to internal file compression. Average data file size is approximately $40\,\mathrm{MB}$. A full day of data averages approximately $2\,\mathrm{GB}$. The *rSIR-SMAP* data product at NSIDC includes SMAP data from 31 Mar 2015 to 06 Apr 2019. The total data volume delivered to NSIDC is $2.7\,\mathrm{TB}$. The SMAP radiometer continues to operate as of the date of this document. We are actively seeking financial support to extend the data coverage.

6 References

References

Backus, G. and F. Gilbert. 1968. The Resolving Power of Gross Earth Data. *Geophysical Journal International 16*(2), 169–205. doi:https://doi.org/10.1111/j.1365-246X.1968.tb00216.x.

Backus, G. and F. Gilbert. 1970. Uniqueness in the inversion of inaccurate gross earth data. *Philosophical Transactions of the Royal Society of London. Series A, Mathematical and Physical Sciences 266*(1173), 123–192. doi:https://doi.org/10.1098/rsta.1970.0005.

Backus, G. E. and J. F. Gilbert. 1967. Numerical Applications of a Formalism for Geophysical Inverse Problems. *Geophysical Journal International 13*(1-3), 247–276. doi:https://doi.org/10.1111/j.1365-246X.1967.tb02159.x.

Brodzik, M. J., B. Billingsley, T. Haran, B. Raup, and M. H. Savoie. 2012. EASE-Grid 2.0: Incremental but Significant Improvements for Earth-Gridded Data Sets. *ISPRS Int. J. Geo-Inf. 1*, 32–45. doi:https://doi.org/10.3390/ijgi101003.

Brodzik, M. J., B. Billingsley, T. Haran, B. Raup, and M. H. Savoie. 2014. Correction: Brodzik, M.J., *et al.* EASE-Grid 2.0: Incremental but Significant Improvements for Earth-Gridded Data Sets, *ISPRS Int. J. Geo-Inf.* 2012, 1, 32–45. *ISPRS Int. J. Geo-Inf. 3*, 1154–1156. doi:https://doi.org/10.3390/ijgi3031154.

Brodzik, M. J. and K. Knowles. 2011. EASE-Grid 2.0 Land-Ocean-Coastline-Ice Masks Derived from Boston University MODIS/Terra Land Cover Data. NASA National Snow and Ice Data Center DAAC, Boulder, CO USA. Digital Media, http://nsidc.org/data/nsidc-0610, doi:https://doi.org/10.5067/XR8523MC24TB.

Brodzik, M. J. and D. G. Long. 2018. Calibrated Passive Microwave Daily EASE-Grid 2.0 Brightness Temperature ESDR (CETB) Algorithm Theoretical Basis Document, v1.0. MEaSUREs Project White Paper. National Snow and Ice Data Center. Boulder, CO. Accessed 2018–08–01 at http://nsidc.org/pmesdr/files/2018/05/MEaSUREs_CETB_ATBD_v1.0.pdf.

Brodzik, M. J., D. G. Long, and M. A. Hardman. 2019. SMAP Radiometer Twice–Daily rSIR–Enhanced EASE-Grid 2.0 Brightness Temperatures, Version 1.0. NASA National Snow and Ice Data Center DAAC, Boulder, CO USA. Digital Media, http://nsidc.org/data/nsidc-0738, doi:https://doi.org/10.5067/QZ3WJNOUZLFK.

Brodzik, M. J., D. G. Long, M. A. Hardman, A. Paget, and R. L. Armstrong. 2016, updated 2019. MEaSUREs Calibrated Enhanced-Resolution Passive Microwave Daily EASE-Grid 2.0 Brightness Temperature ESDR, Version 1. National Snow and Ice Data Center, Boulder, CO USA. Digital Media http://nsidc.org/data/nsidc-0630, doi:https://doi.org/10.5067/MEASURES/CRYOSPHERE/NSIDC-0630.001.

Brodzik, M. J., J. M. Ramage, M. A. Hardman, D. G. Long, and R. L. Armstrong. 2018. Improving melt onset detection in mountainous regions from the new, enhanced-resolution passive microwave climate record. Poster presentation at EGU General Assembly, CR 2.1:10690, Vienna, Austria, 9–13 April.

Chaubell, J., S. Chan, R. Dunbar, D. Entekhabi, J. Peng, J. Piepmeier, and S. Yueh. 2017, July. Backus–Gilbert Optimal Interpolation Applied to Enhance SMAP Data: Implementation and Assessment. In *2017 IEEE International Geoscience and Remote Sensing Symposium (IGARSS)*, Ft. Worth, TX, USA, pp. 2531–2534. doi:https://doi.org/10.1109/IGARSS.2017.8127510.

Das, N. N., D. Entekhabi, R. S. Dunbar, A. Colliander, F. Chen, W. Crow, T. J. Jackson, A. Berg, D. D. Bosch, T. Caldwell, M. H. Cosh, C. H. Collins, E. Lopez-Baeza, M. Moghaddam, T. Rowlandson, P. J. Starks, M. Thibeault, J. P. Walker, X. Wu, P. E. O'Neill, S. Yueh, and E. G. Njoku. 2018. The SMAP Mission Combined Active–Passive Soil Moisture Product at 9 km and 3 km Spatial Resolutions. *Remote Sensing of Environment 211*, 204–217. doi:https://doi.org/10.1016/j.rse.2018.04.011.

Early, D. S. and D. G. Long. 2001, Feb. Image reconstruction and enhanced resolution imaging from irregular samples. *IEEE Transactions on Geoscience and Remote Sensing 39*(2), 291–302. doi:https://doi.org/10.1109/36.905237.

Entekhabi, D., E. G. Njoku, P. E. O'Neill, K. H. Kellogg, W. T. Crow, W. N. Edelstein, J. K. Entin, S. D. Goodman, T. J. Jackson, J. Johnson, J. Kimball, J. R. Piepmeier, R. D. Koster, N. Martin, K. C. McDonald, M. Moghaddam, S. Moran, R. Reichle, J. C. Shi, M. W. Spencer, S. W. Thurman, L. Tsang, and J. Van Zyl. 2010. The Soil Moisture Active Passive (SMAP) Mission. *Proceedings of the IEEE 98*(5), 704–716.

Entekhabi, D., S. Yueh, P. E. O'Neill, K. H. Kellog, A. Allen, R. Bindlish, et al.. 2014. *SMAP Handbook–Soil Moisture Active Passive: Mapping Soil Moisture and Freeze/Thaw from Space*. Number JPL CL#14-2285. Pasadena, CA, USA: Jet Propulsion Laboratory. https://smap.jpl.nasa.gov/files/smap2/SMAP_Handbook_FINAL_1_JULY_2014_Web.pdf.

Lehner, B. and P. Döll. 2004. Development and Validation of a Global Database of Lakes, Reservoirs and Wetlands. *Journal of Hydrology 296*(1–4), 1–22.

Long, D. G.. 2017. Comparison of SeaWinds Backscatter Imaging Algorithms. *IEEE Journal of Selected Topics in Applied Earth Observations 10*(3), 2214–2231. doi:https://doi.org/10.1109/JSTARS.2016.2626966.

Long, D. G. and M. J. Brodzik. 2016, May. Optimum Image Formation for Spaceborne Microwave Radiometer Products. *IEEE Transactions on Geoscience and Remote Sensing 54*(5), 2763–2779. doi:https://doi.org/10.1109/TGRS.2015.2505677.

Long, D. G., M. J. Brodzik, and M. A. Hardman. 2019. Enhanced–Resolution SMAP Brightness Temperature Image Products. *IEEE Transactions on Geoscience and Remote Sensing 57*(7), 4151–4163. doi:https://doi.org/10.1109/TGRS.2018.2889427.

Long, D. G., M. J. Brodzik, and M. A. Hardman. 2020. Estimating the Effective Resolution of Enhanced Resolution SMAP Brightness Temperature Image Products. *IEEE Transactions on Geoscience and Remote Sensing TBD*(TBD), xxxx–xxxx. To appear, doi:https://doi.org/TBD.

Long, D. G. and D. L. Daum. 1998, March. Spatial resolution enhancement of SSM/I data. *IEEE Transactions on Geoscience and Remote Sensing 36*(2), 407–417. doi:https://doi.org/10.1109/36.662726.

Long, D. G. and R. O. W. Franz. 2016. Band–limited Signal Reconstruction from Irregular Samples with Variable Apertures. *IEEE Transactions on Geoscience and Remote Sensing 54*(4), 2424–2436. doi:https://doi.org/10.1109/TGRS.2015.2501366.

National Research Council. 2008. *Satellite Observations to Benefit Science and Society: Recommended Missions for the Next Decade*. Washington, DC, USA: National Academies Press.

Piepmeier, J., P. Mohammed, G. DeAmici, E. Kim, J. Peng, and C. Ruf. 2016. Algorithm Theortical Basis Document SMAP L1B Radiometer Brightness Temperature Data Product: L1B_TB (Includes L1A and L1B) Rev. B. NASA Goddard Space Flight Center, USA. Digital Media, https://ntrs.nasa.gov/archive/nasa/casi.ntrs.nasa.gov/20160003317.pdf.

Piepmeier, J. R., P. Focardi, K. A. Horgan, J. Knuble, N. Ehsan, J. Lucey, C. Brambora, P. R. Brown, P. J. Hoffman, R. T. French, R. L. Mikhaylov, E. Kwack, E. M. Slimko, D. E. Dawson, D. Hudson, J. Peng, P. N. Mohammed, G. De Amici, A. P. Freedman, J. Medeiros, F. Sacks, R. Estep, M. W. Spencer, C. W. Chen, K. B. Wheeler, W. N. Edelstein, P. E. O'Neill, and E. G. Njoku. 2017. SMAP L–Band Microwave Radiometer: Instrument Design and First Year on Orbit. *IEEE Transactions on Geoscience and Remote Sensing 55*(4), 1954–1966.

Piepmeier, J. R., P. Mohammed, J. Peng, E. J. Kim, G. D. Amici, M. J. Chaubell, and C. Ruf. 2018. SMAP L1B Radiometer Half–Orbit Time–Ordered Brightness Temperatures, Version 4. NASA National Snow and Ice Data Center DAAC, Boulder, CO USA. Digital Media, `http://nsidc.org/data/spl1btb`, doi:`https://doi.org/10.5067/VA6W2M0JTK2N`.

Ulaby, F. T. and D. G. Long. 2014. *Microwave Radar and Radiometric Remote Sensing*. Ann Arbor, MI, USA: University of Michigan Press.

Wessel, P. and W. H. F. Smith. 2015. A Global, Self-Consistent, Hierarchical High–Resolution Geography Database, V2.3.4. Digital Media, `http://www.soest.hawaii.edu/pwessel/gshhg`.

Appendices

A rSIR-SMAP Projections and Grids

Table 6: *rSIR-SMAP 36 km product EASE-Grid 2.0 projections and grid dimensions, produced for compatibility with standard SMAP gridded products.*

Name	Projection	Resolution (km)	Cols	Rows	Latitude Extent	Longitude Extent
EASE2-M36km	Mid- and Low-Latitude Cylindrical	36.032 220 840 584	964	406	±85.044 566 4°	±180°
EASE2-M09km	Mid- and Low-Latitude Cylindrical	9.008 055 210 146	3856	1624	±85.044 566 4°	±180°
EASE2-M03km	Mid- and Low-Latitude Cylindrical	3.002 685 070 048 7	11 568	4872	±85.044 566 4°	±180°
EASE2-N36km	Northern Lambert Azimuthal	36.0	500	500	0°–90°	±180°
EASE2-N09km	Northern Lambert Azimuthal	9.0	2000	2000	0°–90°	±180°
EASE2-N03km	Northern Lambert Azimuthal	3.0	6000	6000	0°–90°	±180°
EASE2-S36km	Southern Lambert Azimuthal	36.0	500	500	−90°–0°	±180°
EASE2-S09km	Southern Lambert Azimuthal	9.0	2000	2000	−90°–0°	±180°
EASE2-S03km	Southern Lambert Azimuthal	3.0	6000	6000	−90°–0°	±180°

Table 7: *rSIR-SMAP 25 km product EASE-Grid 2.0 projections and grid dimensions, produced for compatibility with CETB ESDR data products (Brodzik et al., 2019).*

Name	Projection	Resolution (km)	Cols	Rows	Latitude Extent	Longitude Extent
EASE2-T25km	Temperate and Tropical Cylindrical	25.025 260 00	1388	540	±67.057 640 6°	±180°
EASE2-T3.125km	Temperate and Tropical Cylindrical	3.128 157 50	11 104	4320	±67.057 640 6°	±180°
EASE2-N25km	Northern Lambert Azimuthal	25.0	720	720	0°–90°	±180°
EASE2-N3.125km	Northern Lambert Azimuthal	3.125	5760	5760	0°–90°	±180°
EASE2-S25km	Southern Lambert Azimuthal	25.0	720	720	−90°–0°	±180°
EASE2-S3.125km	Southern Lambert Azimuthal	3.125	5760	5760	−90°–0°	±180°

B rSIR-SMAP Data Definition

B.1 File Requirements

Following Brodzik et al. (2019), rSIR-SMAP product file requirements include:

- Output file format shall be acceptable for NSIDC DAAC to easily ingest to ECS
- File size maximum will be $< 1\,\mathrm{GB}$ (larger files are allowed in ECS, but fast network speeds cannot always be assumed)
- Files will conform to netCDF-CF 1.6 conventions for all but the requirement that puts the lat/lon arrays into the file; however, we will include CF-compliant coordinate variables with projected coordinate locations
- Files should pass CF-compliance-checking for all but the lat/lon arrays (we used JPL compliance-checker)
- Each file will contain 1 T_B array variable, with associated ancillary variables, possibly different ancillary variables for each gridding technique. We may have a practical limit on the number of ancillary variables to include, limited by maximum file size
- Each file of the same type (GRD, rSIR, or BGI) will contain the same file-level metadata for that type. e.g. an rSIR file will contain different tuning parameters than a BGI file, but all rSIR files will contain consistent metadata
- We will follow the DRY (Don't Repeat Yourself) principle: Metadata will not be duplicated at multiple places in the same file
- DRY exception: Time values will be machine- and human-readable
- DRY exception: Some projection metadata may be in multiple forms (a proj4 string and/or a WKT string)
- Variable/attribute names will be CF-compliant whenever possible

The rSIR-SMAP .nc files work with gdal utility, *gdal_translate*, to produce a geoTIFF version of each of the data variables <variable_name> in the file, (details in Brodzik et al. (2018)), for e.g.:

```
$ gdal_translate -of GTiff -b 1 \
NETCDF:''cetb.nc'':<variable_name> variable_name.tif
```

B.2 Filename Convention

rSIR-SMAP data are distributed by the NSIDC DAAC (http://nsidc.org/data/nsidc-0738). Filenames are:
<product_id>-<grid_name>-<platform_sensor>-<yyyyddd>
-<channel_id>-<pass>-<algorithm>-<input_source>-<version>.nc
where parts of the filename are described in Table 8.

Table 8: *rSIR-SMAP file naming convention*

Part	Description	Values
<product_id>	NSIDC unique data product id	NSIDC-0738
<grid_name>	EASE-Grid 2.0 grid id	See Tables 6 and 7
<platform>	Satellite platform	SMAP
<sensor>	Sensor name	LRM
<yyyyddd>	Date	4-digit year and 3-digit day-of-year
<channel_id>	Channel (frequency in GHz and polarization)	1.4 followed by polarization, one of: • H = horizontal • V = vertical • F = Fourth Stoke's parameter
<pass>	Pass direction (M or T grids) or ltod (N or S grids)	one of: • A = Ascending • D = Descending • M = Morning • E = Evening
<algorithm>	Reconstruction algorithm	one of GRD or SIR
<input_source>	Data producer	JPL
<version>	Version number	production version number

B.3 File Content, v1.x

Following are sample NetCDF *ncdump –h* utility output, describing a sample example v1.x SIR file. File-level metadata and processing details vary depending on projection, spatial resolution and processing details (method, input file list, etc.).

```
netcdf NSIDC-0738-EASE2_M09km-SMAP_LRM-2019090-1.4V-A-SIR-JPL-v1.0 {
dimensions:
   time = UNLIMITED ; // (1 currently)
   y = 1624 ;
   x = 3856 ;
variables:
   double time(time) ;
      time:standard_name = "time" ;
      time:coverage_content_type = "coordinate" ;
```

```
      time:long_name = "ANSI date" ;
      time:units = "days since 1972-01-01 00:00:00" ;
      time:calendar = "gregorian" ;
      time:axis = "T" ;
      time:valid_range = 0., 1.79769313486232e+308 ;
   double y(y) ;
      y:standard_name = "projection_y_coordinate" ;
      y:coverage_content_type = "coordinate" ;
      y:long_name = "y" ;
      y:units = "meters" ;
      y:axis = "Y" ;
      y:valid_range = -7314540.83063855, 7314540.83063855 ;
   double x(x) ;
      x:standard_name = "projection_x_coordinate" ;
      x:coverage_content_type = "coordinate" ;
      x:long_name = "x" ;
      x:units = "meters" ;
      x:axis = "X" ;
      x:valid_range = -17367530.4451615, 17367530.4451615 ;
   char crs ;
      crs:inverse_flattening = 298.257223563 ;
      crs:semi_major_axis = 6378137. ;
      crs:srid = "urn:ogc:def:crs:EPSG::6933" ;
      crs:longitude_of_central_meridian = 0. ;
      crs:standard_parallel = 30. ;
      crs:proj4text = "+proj=cea +lat_0=0 +lon_0=0
+lat_ts=30 +x_0=0 +y_0=0 +ellps=WGS84 +datum=WGS84 +units=m" ;
      crs:references = "[\"EASE-Grid 2.0 documentation: ...
      crs:false_northing = 0. ;
      crs:grid_mapping_name = "lambert_cylindrical_equal_area" ;
      crs:crs_wkt = "PROJCRS[\"WGS 84 / NSIDC EASE-Grid 2.0 Global...
      crs:false_easting = 0. ;
      crs:coverage_content_type = "auxiliaryInformation" ;
      crs:long_name = "EASE2_M09km" ;
   ushort TB(time, y, x) ;
      TB:standard_name = "brightness_temperature" ;
      TB:long_name = "SIR TB" ;
      TB:units = "K" ;
      TB:_FillValue = 0US ;
      TB:missing_value = 60000US ;
```

```
      TB:valid_range = 5000US, 35000US ;
      TB:packing_convention = "netCDF" ;
      TB:packing_convention_description = "unpacked = ...
      TB:scale_factor = 0.01f ;
      TB:add_offset = 0.f ;
      TB:grid_mapping = "crs" ;
      TB:coverage_content_type = "image" ;
      TB:sir_number_of_iterations = 25 ;
      TB:median_filter = 0 ;
      TB:measurement_response_threshold_dB = -8.f ;
      TB:measurement_search_bounding_box_km = 252.2256f ;
      TB:temporal_division = "Ascending" ;
      TB:frequency_and_polarization = "1.4V" ;
   ubyte TB_num_samples(time, y, x) ;
      TB_num_samples:long_name = "SIR TB Number of Measurements" ;
      TB_num_samples:units = "count" ;
      TB_num_samples:_FillValue = 0UB ;
      TB_num_samples:valid_range = 1UB, 255UB ;
      TB_num_samples:flag_values = 255UB ;
      TB_num_samples:flag_meanings = "num_samples GE 255" ;
      TB_num_samples:grid_mapping = "crs" ;
      TB_num_samples:coverage_content_type = "auxiliaryInformation" ;
   short Incidence_angle(time, y, x) ;
      Incidence_angle:standard_name = "angle_of_incidence" ;
      Incidence_angle:long_name = "SIR Incidence Angle" ;
      Incidence_angle:units = "degree" ;
      Incidence_angle:_FillValue = -1s ;
      Incidence_angle:valid_range = 0s, 9000s ;
      Incidence_angle:packing_convention = "netCDF" ;
      Incidence_angle:packing_convention_description = "unpacked...
      Incidence_angle:scale_factor = 0.01f ;
      Incidence_angle:add_offset = 0.f ;
      Incidence_angle:grid_mapping = "crs" ;
      Incidence_angle:coverage_content_type = "auxiliaryInformation" ;
   ushort TB_std_dev(time, y, x) ;
      TB_std_dev:long_name = "SIR TB Std Deviation" ;
      TB_std_dev:units = "K" ;
      TB_std_dev:_FillValue = 65535US ;
      TB_std_dev:missing_value = 65534US ;
      TB_std_dev:valid_range = 0US, 65533US ;
```

```
      TB_std_dev:packing_convention = "netCDF" ;
      TB_std_dev:packing_convention_description = "unpacked...
      TB_std_dev:scale_factor = 0.01f ;
      TB_std_dev:add_offset = 0.f ;
      TB_std_dev:grid_mapping = "crs" ;
      TB_std_dev:coverage_content_type = "auxiliaryInformation" ;
   short TB_time(time, y, x) ;
      TB_time:standard_name = "time" ;
      TB_time:long_name = "SIR TB Time of Day" ;
      TB_time:units = "minutes since 2019-03-31 00:00:00" ;
      TB_time:_FillValue = -32768s ;
      TB_time:valid_range = -32767s, 32767s ;
      TB_time:packing_convention = "netCDF" ;
      TB_time:packing_convention_description = "unpacked...
      TB_time:scale_factor = 1.f ;
      TB_time:add_offset = 0.f ;
      TB_time:grid_mapping = "crs" ;
      TB_time:coverage_content_type = "auxiliaryInformation" ;
      TB_time:calendar = "gregorian" ;

// global attributes:
   :Conventions = "CF-1.6, ACDD-1.3" ;
   :title = "SMAP Radiometer Twice-Daily rSIR-Enhanced
EASE-Grid 2.0 Brightness Temperatures" ;
   :product_version = "v1.0" ;
   :software_version_id = "1.0.5" ;
   :software_repository = "git@bitbucket.org:nsidc/measures-byu.git" ;
   :history = "meas_meta_sir" ;
   :comment = "Epoch date for data in this file: 2019-03-31 00:00:00Z" ;
   :source = "10.5067/VA6W2M0JTK2N : See input_fileN
list and number_of_input_files attributes" ;
   string :references = "Long, D. G., M. J. Brodzik and M. A. Hardman...
   :metadata_link = "http://nsidc.org/data/nsidc-0738.html" ;
   :summary = "Enhanced-resolution, gridded SMAP L-band ...
   string :institution = "National Snow and Ice Data Center...
   :publisher_name = "NASA National Snow and Ice...
   :publisher_type = "institution" ;
   :publisher_url = "http://nsidc.org" ;
   :publisher_email = "nsidc@nsidc.org" ;
   :program = "NASA 2016 ROSES (Research
```

```
Opportunities in Space and Earth Science) SUSMAP (Science Utilization of SMAP)" ;
   :project = "Improved, enhanced-resolution SMAP
soil moisture using image reconstruction" ;
   :standard_name_vocabulary = "CF Standard Name Table (v27, 28 November 2013)" ;
   :cdm_data_type = "Grid" ;
   :keywords = "EARTH SCIENCE > SPECTRAL/ENGINEERING
> MICROWAVE > BRIGHTNESS TEMPERATURE" ;
   :keywords_vocabulary = "NASA Global Change Master
Directory (GCMD) Earth Science Keywords, Version 8.5" ;
   :platform = "SMAP > Soil Moisture Active and Passive Observatory" ;
   :platform_vocabulary = "NASA Global Change Master
Directory (GCMD) Earth Science Keywords, Version 8.5" ;
   :instrument = "SMAP L-BAND RADIOMETER > SMAP L-Band Radiometer" ;
   :instrument_vocabulary = "NASA Global Change
Master Directory (GCMD) Earth Science Keywords, Version 8.5" ;
   :time_coverage_resolution = "P1d" ;
   :geospatial_lat_units = "degree_north" ;
   :geospatial_lon_units = "degree_east" ;
   :geospatial_x_units = "meters" ;
   :geospatial_y_units = "meters" ;
   :naming_authority = "org.doi.dx" ;
   :id = "10.5067/QZ3WJNOUZLFK" ;
   :date_created = "2019-07-01T15:07:09MDT" ;
   :date_modified = "2019-07-01T15:07:09MDT" ;
   :date_issued = "2019-07-01T15:07:09MDT" ;
   :date_metadata_modified = "2019-07-01T15:07:09MDT" ;
   :input_data_quality_filtering = "Only used highest-quality input data." ;
   string :acknowledgement = "This data set was
created with funding from NASA ROSES SUSMAP Grant
#NNX16AN02G.\n", "Data archiving and distribution is supported by
the NASA NSIDC Distributed Active Archive Center (DAAC)." ;
   :license = "No constraints on data access or use" ;
   :processing_level = "Level 3" ;
   :creator_name = "Mary J. Brodzik" ;
   :creator_type = "person" ;
   :creator_email = "brodzik@nsidc.org" ;
   :creator_url = "http://nsidc.org/pmesdr" ;
   string :creator_institution = "National Snow and Ice Data...
   :contributor_name = "Mary J. Brodzik, David G. Long, Molly A. Hardman" ;
   :contributor_role = "Principal Investigator, Co-Investigator, Developer" ;
```

```
   string :citation = "Brodzik, M. J., D. G. Long,
M. A. Hardman. 2019.\n", "SMAP Radiometer Twice-Daily
rSIR-Enhanced EASE-Grid 2.0 Brightness Temperatures.\n", "Version
1.0.\n", "[Indicate subset used].\n", "Boulder, Colorado USA:
NASA DAAC at the National Snow and Ice Data Cente
r." ;
   :geospatial_bounds = "POLYGON((-85.0445664
-180.000000, -85.0445664 180.000000, 85.0445664 180.000000,
85.0445664 -180.000000, -85.0445664 -180.000000))" ;
   :geospatial_bounds_crs = "EPSG:6933" ;
   :geospatial_lat_min = -85.0445664 ;
   :geospatial_lat_max = 85.0445664 ;
   :geospatial_lon_min = -180. ;
   :geospatial_lon_max = 180. ;
   :geospatial_x_resolution = "9008.06 meters" ;
   :geospatial_y_resolution = "9008.06 meters" ;
   :time_coverage_start = "2019-03-31T00:00:00.00Z" ;
   :time_coverage_end = "2019-03-31T23:38:00.33Z" ;
   :time_coverage_duration = "P00T23:38:00.33" ;
   :number_of_input_files = 15 ;
   :input_file1 =
"SMAP_L1B_TB_22222_A_20190330T235023_R16022_001.h5 (GSX_version:2.0.0)" ;
   :input_file2 = ...
...
   :input_file15 =
"SMAP_L1B_TB_22236_A_20190331T224850_R16022_001.h5 (GSX_version:2.0.0)" ;
}
```

C Effective Resolution

C.1 Pixel Spatial Response Function

As noted earlier, the MRF describes the spatial characteristics of an individual measurement, that is, how much the T_B at each spatial location contributes to the measurement. Analogously, the pixel spatial response function (PSRF) describes the spatial characteristics of the estimated pixel, that is, how much the T_B measurement at a particular spatial location contributes to the reported brightness temperature of the pixel. In effect, the PSRF is the impulse response of the measurement system, including the image formation from (possibly) multiple measurements, while the MRF is the impulse response of a single measurement. Analysis of the PSRF yields an estimate of the effective resolution of the image formation.

Computation of the PSRF can be done using the MRFs of the individual measurements combined into the pixel value. The PSRF will vary from pixel to pixel, due to the differences in location of the measurements within the pixel area and variations in the MRFs for the measurements (Long et al., 2019). The variation in the MRFs precludes the use of classic deconvolution algorithms that required a fixed response function. Typically, the PSRF is normalized to a peak value of 1.

The pixel value of simple image formation algorithms such as DIB is derived from the linear sum of measurements included in the pixel value (Long and Brodzik, 2016). Similarly, for resampling or interpolation, the PSRF is calculated from the weighted linear sum of the measurement MRFs included in the pixel value. This value includes effects of the offsets of each measurement from the pixel center and from each other (Long and Brodzik, 2016, Long, 2017). Due to the non-linearity in rSIR, this approach cannot be used. As an alternative to the simulation approach to compute the PSRF using a simulated impulse function, we can estimate the PSRF from actual data.

C.2 Relationship of PSRF to Effective Resolution

Given the PSRF, the effective resolution of an image corresponds to the area of the PSRF greater than a particular threshold, typically $3\,\mathrm{dB}$ (Long and Brodzik, 2016). The resolution is often expressed in terms of the square root of the area, hereafter we use the term "linear resolution". For example, the ideal PSRF for a rectilinear image is a two-dimensional "rect" or "box-car" function that is one over the pixel and zero elsewhere, (Figure 13). For an image of $36\,\mathrm{km}$ square pixels, the ideal "pixel resolution" is $1296\,\mathrm{km}^2$, which is a linear resolution of $36\,\mathrm{km}$. According to the Nyquist criterion, the finest spatial frequency that can be represented with pixel values spaced $36\,\mathrm{km}$ apart is then $1/72\,\mathrm{km}^{-1}$, that is, the wavelength of the finest representable spatial frequency is $72\,\mathrm{km}$.

Since only a finite number of discrete measurements are available, we assume that the

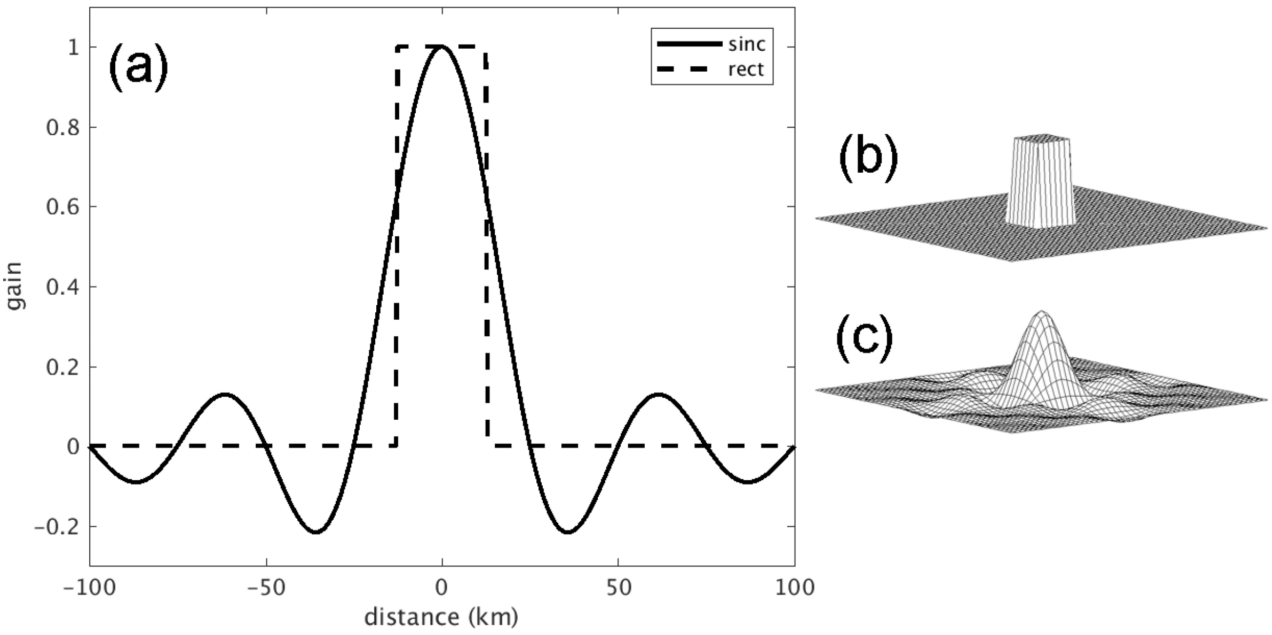

Figure 13: *Example plots of one-dimensional (a) and two-dimensional rect (b) and sinc (c) functions.*

signal and the PSRF are bandlimited consistent with the sample spacing (Long and Franz, 2016). A bandlimited version of the ideal boxcar PSRF is a two-dimensional sinc function, (Figure 13). For ideal $36\,\mathrm{km}$ sampling, this bandlimited PSRF is the best achievable PSRF that is consistent with the sampling. By the Nyquist criterion, signals with frequency higher than twice the sampling rate cannot be represented without aliasing.

The spacing of the pixels is sometimes called the *posting resolution*. In general, the pixels can be larger than their spacing so that the pixels overlap. In this case, the pixel size is larger than the posting resolution. A common way to specify the effective microwave image resolution is the width when the PSRF is greater than $1/2\,,$ also known as the $3\,\mathrm{dB}$ PSRF size. The effective resolution, ($-3\,\mathrm{dB}$ PSRF size), is typically larger than than the pixel size, and thus is larger than the posting resolution. Note that if we choose a smaller PSRF size threshold, e.g., $-10\,\mathrm{dB}$ instead of $-3\,\mathrm{dB}$, the effective area is even larger. When the posting resolution is finer than the effective resolution the signal is sometimes termed *oversampled*. In these cases the image can, in principle, be resampled to a coarser posting resolution with no loss of information. Our decision to report images at standard posting resolutions with pixel sizes that are oversampled provides the most flexibility to users in resampling the data.

One way to determine the effective resolution is based on estimating the step response of the imaging process. We assume the PSRF is symmetric, so the PSRF can be derived from the observed step response. This simplifies the process of estimating the effective resolution.

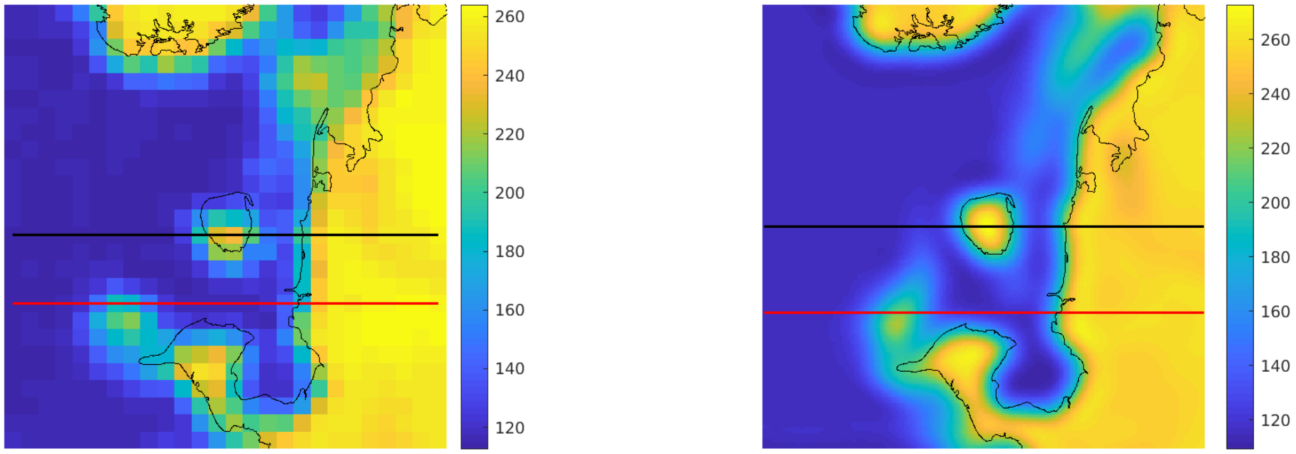

Figure 14: *20-day average of daily vertically-polarized SMAP T_B images over study area, 2015, day 91-110 for 25 km GRD (left) and 3.125 kmrSIR (right). Horizontal lines indicate image transect used for "island-crossing" (black) and "coastline-crossing" (red) analyses. Apparent offset of island in GRD image from coastlines (thin black, from Wessel and Smith (2015)) results from coarse resolution.*

The step response is mathematically the convolution of the PSRF with a step function. The PSRF can thus be computed from the step response by deconvolution with a step function. In this case, the deconvolution product represents a slice of the PSRF. The effective linear resolution is the dimension of the PSRF above the $3\,\mathrm{dB}$ threshold.

C.3 Resolution Estimation Using SMAP Data

We evaluate the effective linear resolution of SMAP image data from actual T_B measurements using SMAP daily images at both conventional and enhanced resolution by estimating the pixel step response. We arbitrarily select a small $200\,\mathrm{km} \times 200\,\mathrm{km}$ region centered at approximately $69N$ and $49E$ in the Arctic Ocean (Figure 14. The cold ocean/warm land transitions provide sharp discontinuities that can be simply modeled. *Ostrov Kolguyev* is a nominally flat, nearly-circular, tundra-covered island that is approximately $81\,\mathrm{km}$ in diameter, with a maximum elevation of approximately $120\,\mathrm{m}$. Since there is variability (noise) from pass to pass, average results over a 20-day time period were considered. The data time period was arbitrarily selected with image T_B values that vary only minimally over the time period, with high contrast between land and ocean.

Two horizontal transects of the study region are considered in separate cases. One crosses the island and the coast, while the second crosses a patch of sea ice and the coast (Figure 15). Due to the dynamics of the sea ice further from the shore, only the near-coast region is considered. We model the surface brightness temperature as essentially constant,

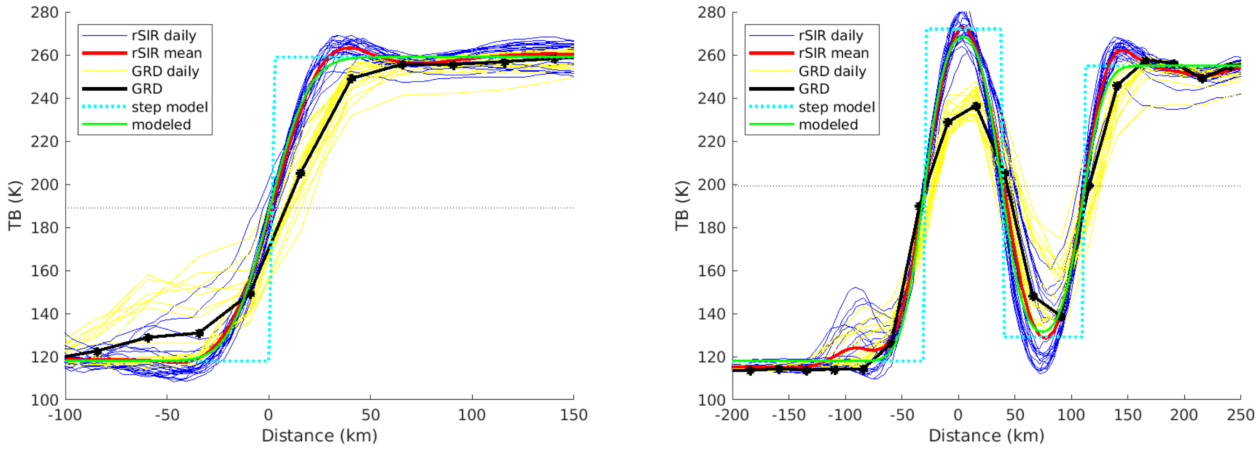

Figure 15: *Plots of T_B along "coast-crossing" (left) and "island-crossing" (right) transect cases in Figure 14. Daily values for the study period shown for rSIR (blue) and GRD (yellow). 20-day averages of each in red and black, respectively. The discrete step (dotted green) and convolved Gaussian step (green) models are also included. X-axis is positioned on the rSIR-derived coastline or island center for the particular case.*

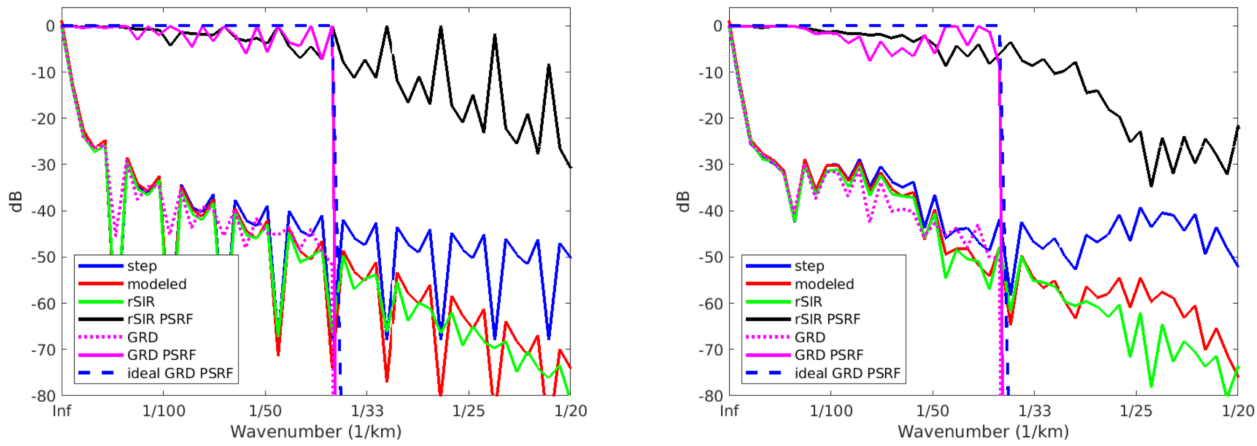

Figure 16: *Wavenumber spectra of T_B slices, the model, and the PSRF for "coast-crossing" (left) and "island-crossing" (right) transect cases.*

with different values over land and water.

Figure 14 compares 20-day averaged daily GRD and rSIR images of the study region. In these images, the cooler (darker) areas are open ocean. Land areas are warmer, with sea-ice covered areas exhibiting a somewhat lower T_B. The GRD images are blocky, while the enhanced-resolution images exhibit finer resolution and more accurately match the coastline. Average images over 20 days of daily TB images are used in order to minimize noise-like effects due to (1) T_B measurement noise and (2) the effects of the variation in measurement locations within each pass and from pass to pass. The derived PSRF and linear resolution thus rep- resent temporal averages. The derived PSRFs are representative of single-pass PSRFs in other areas.

In Figure 14, the ocean and land values are reasonably modelled by different constants, with a transition zone at the coastline. As expected, the GRD images are much blockier than the rSIR images. This is due to the finer grid used to compute the rSIR images and their better effective resolution. Due to the coarse quantization of the grid in the GRD image, the island looks somewhat offset downward whereas the rSIR image better corresponds to the superimposed coastline map.

Figure 15 plots the image T_B value along the two study transects. The rSIR T_Bs have sharper transitions from land to ocean than the GRD images and the GRD image underestimates the island T_B. The GRD values also have longer ocean-side transitions than rSIR and overestimate T_B in *Pomorskiy Proliv*, the strait separating the island and coastline south (right) of the island. On the other hand, the rSIR curves appear to exhibit a small under- and over-shoot near the transitions. Lacking high resolution true T_B maps, it is difficult to precisely analyze the accuracy and resolution of the images. However, we employ signal processing considerations to infer the expected behavior of the values.

We define a simple step model for the underlying T_B. Noting that the T_B variation over land near the coast in the coastline case is a nearly constant $260\,\mathrm{K}$, with a variation no more than a few K, we model the land as a constant $260\,\mathrm{K}$. Similarly, the ocean T_B is modeled as a constant $120\,\mathrm{K}$. The modelled T_B is plotted in Figure 15 for comparison with the observed and reconstructed values. The model T_B is filtered with a $36\,\mathrm{km}$ Gaussian response filter, shown in green, for comparison. The latter represents the "ideal" result that is the best that can be achieved from the model T_B.

We observe that rSIR images have sharper transitions than the GRD images and the GRD image underestimates the island T_B. The GRD images have longer ocean-side transitions than rSIR and overestimate T_B in the strait separating the island and coastline. The ripple artifacts in the rSIR T_B transition from ocean to land in both examples are the result of the implicit low pass filtering in the reconstruction. The pass-to-pass variability in the T_B observations is approximately the same for both GRD and rSIR in most places, suggesting there is not a significant noise penalty when employing rSIR reconstruction for SMAP.

Figure 16 presents the wavenumber spectra of the key signals in Figure 15. Spectra were computed by zero padding the data. For simplicity, only the Fourier transforms of the

average curves are shown. The spectra of the modeled signal is shown in blue. Peaking at 0 wavenumer, it tapers off at higher wavenumbers. The filtered model signal, shown in red, represents the best signal that can be recovered. The GRD signal follows the ideal well until it reaches the $1/36\,\mathrm{km}^{-1}$ cutoff frequency permitted by the grid, beyond which it cannot represent the signal further. rSIR follows this signal out to the limit of the graph and thus has higher effective resolution than GRD, even though the total energy in the signal is small at this level. Details of high wavenumber response differ between the coast-crossing and island-crossing case, but the same conclusions apply.

Deconvolution of the step response is accomplished in the frequency domain by dividing the step response by the spectra of the modelled step function, with care for how zeros and near-zeros in the modelled step function are handled in the inverse operation. The ideal GRD PRSF (blue dashed line) is a rect that cuts off at $1/36\,\mathrm{km}^{-1}$. The estimated GRD PSRF spectrum closely matches the ideal. The rSIR PSRF spectrum also matches the ideal in the low frequency region, but also contains additional information at higher wavenumbers, which gradually rolls off. This additional spectral content provides the finer resolution of rSIR compared to the GRD result.

Table 9: *Inferred linear resolutions from Figure 17, by threshold.*

	$-3\,\mathrm{dB}$ Threshold		$-2\,\mathrm{dB}$ Threshold		$-10\,\mathrm{dB}$ Threshold	
Algorithm	Coast	Island	Coast	Island	Coast	Island
Gauss	34.4	34.4	28.1	28.1	64.1	64.1
rSIR	49.2	38.7	35.2	31.6	80.5	65.2
ideal GRD	43.0	43.0	35.1	35.9	64.8	64.8
GRD	52.3	53.5	43.4	44.1	85.5	90.6

Finally, Figure 17 plots the estimated one-dimensional PSRFs computed as the inverse Fourier transform of the PSRF spectra in Figure 16. Table 9 lists the linear resolution for each, computed as the width of the PSRF at the $-3\,\mathrm{dB}$ point. For comparison, the linear resolution using both $-2\,\mathrm{dB}$ and $-10\,\mathrm{dB}$ thresholds is shown. In all cases the resolution of rSIR is better than the observed GRD resolution.

We note that the effective resolution, as defined by the $3\,\mathrm{dB}$ width of the derived PSRFs, is very similar for both analysis cases. As expected, the observed GRD PSRF results are coarser than the ideal GRD PSRFs, due to the extension of the MRFs outside of the pixel area. The rSIR curve has a small shoulder on the right side which makes it asymmetric and wider in the coastal case than the island case, but otherwise the rSIR PSRF nearly matches the Gaussian-filtered model over the main lobe. The island crossing rSIR result has finer linear resolution than the both the ideal GRD and actual GRD results. The island rSIR resolution represents an improvement of nearly $30\,\%$ compared with the observed GRD resolution and $10\,\%$ from the ideal GRD resolution. We conclude that rSIR does, in fact,

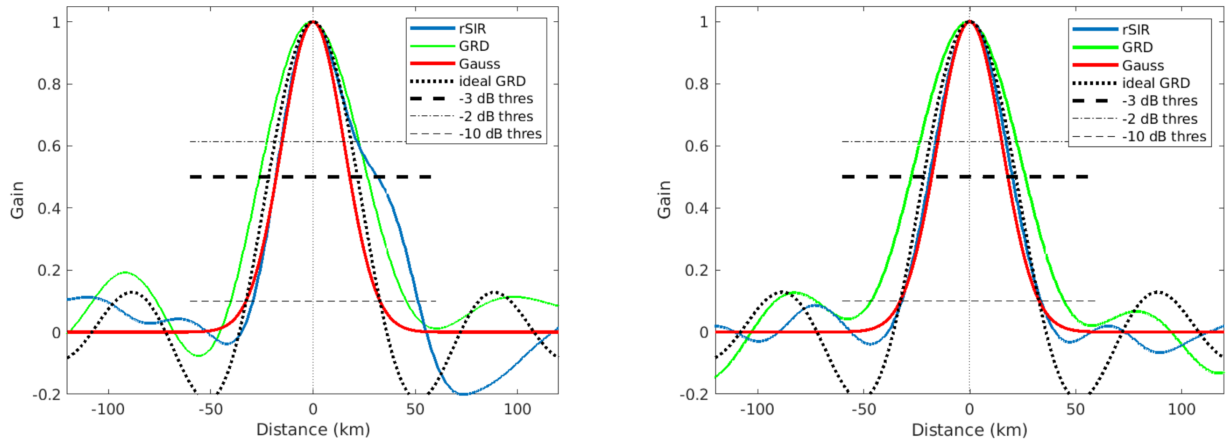

Figure 17: *Derived single-pass PSRFs for "coast-crossing" (left) and "island-crossing" (right) cases. Also included for comparison are the 36-km wide Gaussian window and 36-km wide sinc function, which represents the ideal GRD pixel PSRF. Horizontal dashed lines correspond to -3 dB, -2 dB and -10 dB thresholds. The effective 3 dB linear resolution is the width of the PSRF at this line.*

provide finer effective resolution than GRD products, with an improvement of nearly $30\,\%$.